

Evaluation of a Quasi-steady state approximation of the cloud Droplet Growth Equation (QDGE) scheme for aerosol activation in global models using multiple aircraft data over both continental and marine environments

5 Hengqi Wang¹, Yiran Peng¹, Knut von Salzen², Yan Yang³, Wei Zhou³, Delong Zhao³

¹Department of Earth System Science, Ministry of Education Key Laboratory for Earth System Modeling, Institute for Global Change Studies, Tsinghua University, Beijing 100084, China

²Canadian Centre for Climate Modelling and Analysis, Environment and Climate Change Canada, Victoria, British Columbia, Canada

10 ³Beijing Weather Modification Office, Beijing, 100101, China

Correspondence to: Yiran Peng (pyiran@mail.tsinghua.edu.cn) and Knut von Salzen (Knut.vonSalzen@ec.gc.ca)

Abstract. This research introduces a numerically efficient aerosol activation scheme and evaluates it by using stratus and stratocumulus cloud data sampled during multiple aircraft campaigns in Canada, Chile, Brazil, and China. The scheme employs a Quasi-steady state approximation of the cloud Droplet Growth Equation (QDGE) to efficiently simulate aerosol activation, the vertical profile of supersaturation, and the activated cloud droplet number concentration (*CDNC*) near the cloud base. The calculated maximum supersaturation values using the QDGE scheme were compared with multiple parcel model simulations under various aerosol and environmental conditions. The differences are all below 0.18 %, indicating good performance and accuracy of the QDGE scheme. We evaluated the QDGE scheme by specifying observed environmental thermodynamic variables and aerosol information from 31 cloud cases as input and comparing the simulated *CDNC* with cloud observations. The average of mean relative error (\overline{MRE}) of the simulated *CDNC* for cloud cases in each campaign ranges from 17.30 % in Brazil to 25.90 % in China, indicating that the QDGE scheme successfully reproduces observed variations in *CDNC* over a wide range of different meteorological conditions and aerosol regimes. Additionally, we carried out an error analysis by calculating the Maximum Information Coefficient (MIC) between the mean relative error (*MRE*) and input variables for the individual campaigns and all cloud cases. MIC values were then sorted by aerosol properties, pollution level, environmental humidity, and dynamic condition according to their relative importance to *MRE*. Based on the error analysis, we found that the magnitude of *MRE* is more relevant to the specification of input aerosol pollution level in marine regions and aerosol hygroscopicity in continental regions than to other variables in the simulation.

1 Introduction

30 Aerosols play an important role in determining the radiation balance of the earth-atmosphere system by scattering and absorbing shortwave radiation and altering the cloud reflectivity and lifetime (Twomey, 1974, 1977; Ghan, 2013; Forster et al., 2016; Ramaswamy et al., 2019; Wang et al., 2020). Currently, aerosol-cloud interactions are one of the largest sources of climate modeling uncertainty (IPCC AR6, Forster et al., 2021).

35 Aerosol-cloud interactions are largely driven by the activation of aerosols to form cloud droplets. The addition of activated aerosol to existing clouds can directly change the concentration and size of cloud droplets and thereby affect the microphysical properties and radiative forcing of the clouds. Aerosol activation is controlled by rapid and nonlinear aerosol and cloud microphysical processes (Meskhidze et al., 2005), which have not been explicitly resolved in climate models yet (Fountoukis et al., 2007; Kang et al., 2015). Nenes et al. (2001) pointed out that the cloud droplet activation process is subject to kinetic limitations, including inertial, evaporation, and deactivation mechanisms, which further adds to the complexity of the aerosol activation.

40 Early parameterizations of aerosol activation in climate models were based on observations and derived through parameter fitting, using the aerosol number or mass concentration or other Cloud Condensation Nuclei (CCN) proxies (e.g., sulfate mass) to empirically determine the activated *CDNC* (Jones et al., 1994; Boucher and Lohmann, 1995; Jones and Slingo, 1996; Lohmann, 1997; Kiehl et al., 2000; Menon et al., 2002). Although these parameterizations have the advantages of convenience and low computational burden (Fountoukis et al., 2007), substantial uncertainties are resulting from limited 45 spatiotemporal representativeness and unresolved variations in aerosol properties (Meskhidze et al., 2005). In the recent two decades, physically-based parameterization schemes of aerosol activation have emerged (Abdul-Razzak and Ghan, 2000; Cohard et al., 2000; Fountoukis and Nenes, 2005; Ming et al., 2006; Kivekäs et al., 2008; Khvorostyanov and Curry, 2009; Shipway and Abel, 2010; Zhang et al., 2015). These schemes are based on the Köhler theory and are used in climate models to parameterize aerosol activation near the cloud base. As Köhler theory fundamentally describes the process by which water 50 vapor condenses and forms liquid cloud droplets, it can be applied to a wide range of atmospheric conditions and aerosol pollution levels. However, considerable approximations of the Köhler theory are employed for application in climate models, which leads to potential biases in comparison with results from more rigorous and accurate simulations of cloud droplet growth with adiabatic parcel models (e.g. Ghan et al. (2011)). The ongoing increase in computing power (Herrington and Reed, 2020) reduces the need for cost-saving approximations in climate models. In the following, we will introduce a Quasi- 55 steady state approximation of the cloud Droplet Growth Equation (QDGE) that provides an efficient alternative to parameterizations of activated *CDNC* in climate models.

Parameterization schemes of aerosol activation have often been evaluated using adiabatic parcel model simulations. These models explicitly solve aerosol activation and droplet growth processes by mimicking vertical uplifting of an air parcel containing a specified number of aerosol particles, predicting changes in temperature, humidity/supersaturation, activation of 60 aerosols, and droplet growth from the cloud base upward. When utilizing identically specified aerosols, the results of a

parcel model can be used as a benchmark to evaluate parameterizations. This approach has been used extensively to evaluate activation schemes (Table 1). However, a less commonly used approach is to evaluate parameterizations by conducting a “closure experiment”, that is, to carry out a parameterized calculation by specifying observed aerosol concentrations and environmental thermodynamic conditions, and then compare the calculated and observed *CDNC* (e.g. Snider and Brenguier, 2000; Guibert et al., 2003; Fountoukis and Nenes, 2005; Kivekäs et al., 2008). Though some parameterizations have been evaluated based on comparisons of simulated and observed *CDNC* from aircraft campaigns, mostly regional data sets have been used for very specific meteorological conditions and pollution levels. It is essential to select a wide range of cloud data for different atmospheric conditions and pollution levels to arrive at meaningful conclusions for global climate model simulations.

In this study, we introduce the QDGE scheme and evaluate it by using cloud data from multiple aircraft campaigns in four different regions over the world, covering marine and continental conditions. This paper is organized as follows. The next section describes the QDGE scheme and Sect. 3 summarizes the data and method used for the closure experiment. Section 4 illustrates the results of the closure experiment and analyzes the sources of simulation errors, followed by conclusions and discussion in Sect. 5.

Table 1. A summary of activation parameterizations and the evaluation methods in previous studies.

Parameterization	Evaluation methods
Abdul-Razzak et al. (1998)	Parcel model
Cohard et al. (2000)	Parcel model
Snider et al. (2003)	Aircraft measurements
Fountoukis and Nenes (2005)	Parcel model; Aircraft measurements
Ming et al. (2006)	Parcel model
Kivekäs et al. (2008)	Other parameterizations; Aircraft measurements
Khvorostyanov and Curry (2009)	Twomey power law (Pruppacher et al., 1998)
Shipway and Abel (2010)	Parcel model

2 QDGE scheme

2.1 Scheme description

Aerosol particles suspended in an air parcel grow into cloud droplets by condensation of water vapor if supersaturation with respect to water exceeds a critical value. In stratus and convective clouds, aerosol activation is particularly efficient in the vicinity of the cloud base, where supersaturation typically reaches its local maximum. Although observations provide evidence that aerosol activation is not limited to the region near the cloud base, this is omitted in the aerosol activation scheme described here, similar to most models and parameterizations.

In order to determine the portion of the aerosols that activate and form cloud droplets, a numerical solution of the condensational droplet growth equation (e.g. Seinfeld and Pandis, 2016) is employed to simulate the growth of an ensemble
 85 of aerosol particles near the cloud base. The number of activated cloud droplets above the cloud base is simulated by solving a series of equations that describe a vertically ascending air parcel containing aerosols. The vertical velocity of the air parcel, w_c (in m s^{-1}), is either specified or parameterized, as described in Sect. 3.2.3.

The change in wet aerosol particle radius, R_{pw} , by condensation of water vapor as a function of the environmental supersaturation (S , e.g. Emanuel, 1994) in the scheme is given by

$$90 \quad R_{pw} \frac{dR_{pw}}{dt} = \frac{S - S_p}{c}, \quad (1)$$

where S_p is the equilibrium supersaturation over the surface of the particle, which is obtained from κ -Köhler theory (Petters and Kreidenweis, 2007):

$$S_p = \frac{A}{R_{pw}} - \frac{B}{R_{pw}^3}, \quad (2)$$

where the parameters A , B , and C account for thermodynamic conditions in the cloud and physiochemical properties of the
 95 aerosol particles and droplets (Appendix A).

As described below, the QDGE scheme solves Eqs. (1) and (2) in combination with energy and moisture budgets to calculate changes in S driven by thermodynamic processes. For instance, the thermodynamic equations underlying the QDGE scheme can be used to obtain the temporal evolution of S in the air during adiabatic ascend near cloud base (Ghan et al., 2011),

$$\frac{dS}{dt} = D w_c - E \frac{dq_w}{dt}, \quad (3)$$

100 where the parameters D and E are weak functions of temperature and pressure, and q_w is the liquid water mixing ratio, which is related to the activated particle size distribution (Appendix A).

Theoretically, each growing aerosol particle will compete with others for the water vapor in the environment, and the particle size increases according to Eq. (1) and affects the environmental supersaturation through Eq. (3). Eqs. (1-3) are coupled in a complex manner thus hardly having an analytical solution. For example, Eq. (3) indicates that the balance between the
 105 enhancement of S due to the air parcel uplifting, and the reduction of S due to the condensation growth of activated particles, leads to a highly non-linear variation of S with time in the ascending parcel of cloudy air. The condensation growth is non-linearly related to the environmental conditions and aerosol properties (Eqs. 1-2). Therefore, a time step much shorter than 1 second is typically required to numerically solve these equations, which implies computational expenses that would prohibit applications in climate models (Khain et al., 2015). For instance, adiabatic ascending parcel models (e.g. Chen et al., 2016;
 110 Peng et al., 2005) to numerically solve Eqs. (1-3) require a very high time resolution, typically with a time step of 10^{-3} to 10^{-4} seconds.

In large-scale stratus clouds, the maximum supersaturation (usually less than 0.2 %) occurs about 100 m above the cloud base, that is, the rate of S change is $0.002 \% \text{ m}^{-1}$ or so. A similar conclusion can be derived from the change of supersaturation and temperature (combined with a lapse rate of atmospheric temperature; Pandis et al. (1990)). Therefore, it

115 is reasonable to assume a scale of several seconds (or meters) at which the supersaturation is approximately constant in the air parcel. Consequently, we use a Quasi-steady state approximation to solve the Droplet Growth Equation (QDGE), which assumes that the local S is approximately constant. Eq. (1) can then be conveniently expressed as follows,

$$\frac{dx}{du} = \delta - a \left(\frac{b}{x^{1/2}} - \frac{1}{x^{3/2}} \right), \quad (4)$$

120 for the time period from t to $t + \Delta t_s$ (Δt_s is a sub-timestep, roughly several tens of seconds), with variable substitutions for particle size, $x = R_{pw}^2/2$, and for time, $u = t|S|/C$, and parameters that are given by:

$$\delta = \begin{cases} -1 & , \quad \text{if } S < 0, \\ 1 & , \quad \text{if } S \geq 0, \end{cases} \quad (5)$$

$$a = \frac{B}{2^{3/2}|S|}, \quad (6)$$

$$b = \frac{2A}{B}. \quad (7)$$

In the QDGE scheme, pre-calculated solutions of Eq. (4) are used, which are provided in the form of look-up tables (LUTs) for different values of a , b , and δ in the model to calculate R_{pw} . The S -dependent parameters a and δ , and u are determined through an iterative procedure for each time step and vertical level near cloud base, as described in the following.

The major steps of the QDGE scheme are shown in Fig. 1. A vertical grid with N_{sub} sub-levels (grid spacing $\Delta z_s = \Delta z/N_{sub}$) is employed in the QDGE scheme, where Δz is the grid spacing in the atmospheric host model, near cloud base (Fig. 1a-b). Calculations are only performed for the first host model grid layer above the cloud base, with typical values $\Delta z_s \approx 1 - 10$ m. 130 The local approximation with constant S applies in each sub-level Δz_s , and a vertical profile of S is eventually obtained within the host model grid Δz (Fig. 1c). The iterative calculation to obtain S at each sub-level is described below.

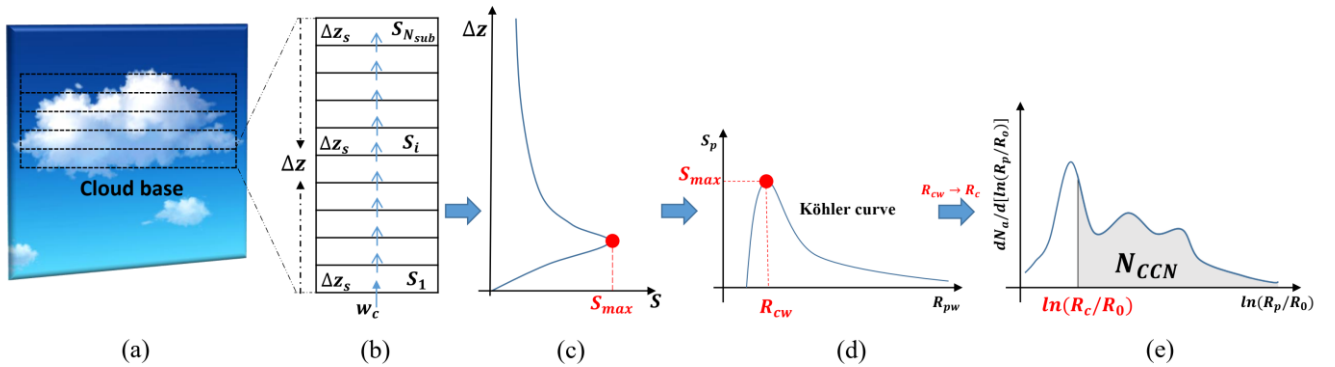


Figure 1. A schematic diagram to show the major steps of the QDGE scheme.

In each sub-level Δz_s , supersaturation (i.e. S_i in Fig. 1b, where $i = 1, \dots, N_{sub}$) and the S -dependent parameters in Eq. (4) are obtained through an iterative calculation, which explicitly requires the conservation of mass and energy. The flow chart of the iterative calculation is shown in Fig. 2. 135

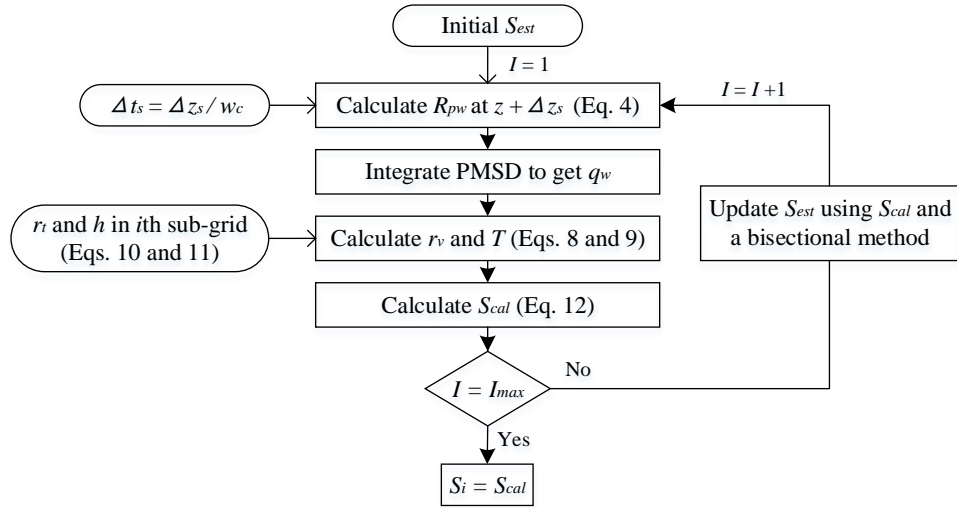


Figure 2. The flow chart of the iterative calculation for the sub-grid supersaturation S_i . I is the number of iterations. PMSD is the particle mass-size distribution. Total water mass mixing ratio, r_t , and liquid water static energy, h , are conserved.

140 At the beginning of an iteration, an initial value of supersaturation (S_{est}) is specified and Eq. (4) is integrated over the sub-timestep $\Delta t_s = \Delta z_s/w_c$ to obtain a first estimate of the particle wet size R_{pw} at the sub-level $z + \Delta z_s$. Next, an integration over the particle mass-size distribution (PMSD) yields a first estimate of the liquid water mixing ratio q_w at $z + \Delta z_s$ (Fig. 2). The subsequent calculations are based on the total water mass mixing ratio, r_t , and liquid water static energy, h , defined as:

$$r_t = r_v + q_w, \quad (8)$$

145 $h = gz + c_p T - L_v q_w,$ (9)

where, r_v is the water vapor mass mixing ratio, T is the temperature, g is the gravitational constant, and c_p is the heat capacity at a constant pressure of dry air. The total water mass mixing ratio and liquid water static energy at the lower and upper boundaries of the current host model grid (with the superscripts L and U respectively) are first calculated using Eqs. (8) and (9). Then, the total water mass mixing ratio (r_t^i) and liquid water static energy (h^i) in the i th sub-level are obtained by

150 linear interpolation, given by

$$r_t^i = \frac{N_{sub}-i+1}{N_{sub}} r_t^L + \frac{i-1}{N_{sub}} r_t^U, \quad (10)$$

$$h^i = \frac{N_{sub}-i+1}{N_{sub}} h^L + \frac{i-1}{N_{sub}} h^U. \quad (11)$$

Knowing r_t^i and h^i , r_v and T in the i th sub-level can be derived from Eqs. (8) and (9) using the estimated q_w . Subsequently, the supersaturation S is calculated, based on the standard definition of the water vapor saturation ratio,

155 $S + 1 = \frac{r_v}{r_*} \left(\frac{1+r_*/\varepsilon}{1+r_v/\varepsilon} \right),$ (12)

where $\varepsilon \equiv 0.622$, and r_* is the saturation water vapor mass mixing ratio in the air parcel, which depends on T .

The calculated supersaturation (S_{cal}) after each iteration is compared to the initial estimate S_{est} . An improved estimate of S is determined using a bisectional method that minimizes the difference between different available estimates of S through iteration, as shown in Fig. 2. The method enables quick convergence to a good-enough estimated value of S , which solves Eq. (4) and satisfies all necessary constraints according to Eqs. (8), (9), and (12). Here, the maximum number of iterations (I_{max}) was set to 4 for the model applications discussed below. The iterations are repeated in each sub-level to calculate S_i until the vertical profile of supersaturation is available at all N_{sub} levels (Fig. 1b).

The maximum value of the simulated vertical supersaturation profile, S_{max} , is used to diagnose the critical particle size, R_{cw} , based on Eq. (2) (Fig. 1c-d). All particles with a radius larger than R_{cw} are taken as the activated particles to become cloud condensation nuclei. Consequently, the cloud condensation nuclei number concentration (N_{CCN}) is obtained by integrating the activated aerosol size distribution accordingly (Fig. 1e). Above cloud base, a uniform number of the activated particles is assumed, equal to the value calculated at cloud base, in good agreement with observations and detailed simulations using cloud resolving models (Gerber et al., 2008; Slawinska et al., 2012; Jarecka et al., 2013).

In each grid of the host model, the dry aerosol number-size distribution is represented as particle numbers at regular size intervals, $\Delta\chi = 1/p\Delta\varphi$, where p is the number of size bins. $\Delta\varphi$ is the particle size range covering both Aitken and accumulation modes, expressed in terms of a dimensionless particle size parameter $\varphi = \ln(R_p/R_0)$, with $R_0 = 10^{-6}$ m. In this study, we set p to 6, meaning that 6 discrete aerosol particle size bins are used. The continuous aerosol size distribution (such as Fig. 1e) can be obtained from linear interpolation using the particle numbers in 6 discrete size bins.

Currently, only adiabatic processes are considered in each sub-level, and therefore total water mass mixing ratio (r_t) and liquid water static energy (h) are conserved as the parcel ascends from z to $z + \Delta z_s$. However, energy and moisture profiles in clouds may be affected by entrainment processes. Therefore, we additionally consider the impact of entrainment on r_t and h above the cloud base by using

$$r_t^{Ue} = r_t^L + (r_t^U - r_t^L)\exp(-e\Delta z), \quad (13)$$

$$h^{Ue} = h^L + (h^U - h^L)\exp(-e\Delta z), \quad (14)$$

where r_t^{Ue} and h^{Ue} are the total water mass mixing ratio and liquid water static energy considering the entrainment of air, with a specified entrainment rate given by e , respectively. These can be used to replace r_t^U and h^U in Eqs. (10) and (11) when entrainment needs to be considered.

Note that Eq. (3) can only be used for an adiabatic process and does not work if there is entrainment or radiative cooling of the air, e.g. the formation of cloud droplets in radiation fog. In contrast, the QDGE scheme is much more general, as outlined above. The QDGE scheme can be easily modified for simulations of entrainment and radiation fog if required.

2.2 Comparison with a parcel model

In this subsection, we examine the performance of the QDGE scheme by comparing it with parcel model results by conducting a series of experiments as described in Ghan et al. (2011). The parcel model can numerically solve the droplet growth equation in a most accurate way by representing aerosol size distributions with finely discretizing bins and utilizing a very short time step to trace the supersaturation variation with time/height (Ghan et al., 2011).

For the comparisons, we assume a tri-modal lognormal size distribution (Whitby, 1978) of ammonium sulfate aerosol, consistent with the experimental setup in Ghan et al. (2011) (Table B1). The environmental conditions in the simulations cover a wide range of w_c values ($0.1 - 10 \text{ m s}^{-1}$) and four different aerosol regimes (Marine, Clean continental, Background, and Urban). When conducting QDGE simulations, we set the number of sub-levels (N_{sub}), the maximal number of iterations (I_{max}), and the number of size bins (p) as 60, 4, and 6, respectively, which are the same as those in the following closure experiment (Sect. 4.1). Comparison between the results from the simulations are shown in Fig. 3, in which the parcel model results are identical to those in Ghan et al. (2011). In general, the QDGE scheme performs well with lower w_c but overestimates the S_{max} when w_c is larger than 2 m s^{-1} . The differences in S_{max} between parcel model and the QDGE scheme in all experiments are within 0.18 % (with an average of 0.05 %), much lower than the differences between parcel model and four state-of-the-art activation schemes (within approximately $\pm 1.5 \%$) in Ghan et al. (2011). This indicates that the QDGE scheme achieves a high accuracy in simulating the processes of activation and condensation growth of cloud droplets under the specified conditions.

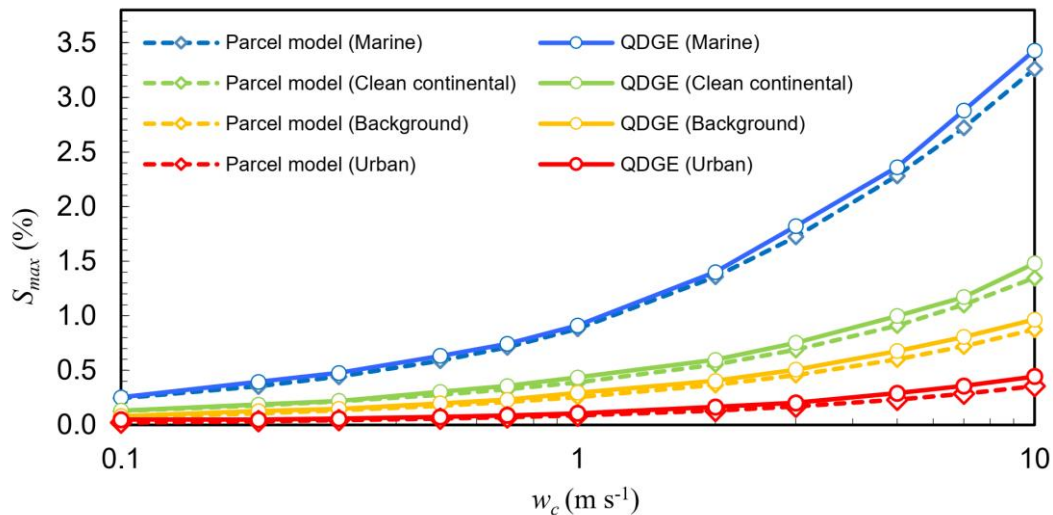


Figure 3. Comparison between the calculated maximum supersaturation (S_{max}) from the QDGE scheme (solid line) and the parcel model (dashed line, Ghan et al., 2011).

In contrast to the QDGE scheme, the four activation schemes considered by Ghan et al. (2011) are based on parameterized and simplifying assumptions about the physical processes involved in the formation of clouds droplets, using the vertical grid of the host model. Therefore, the QDGE scheme can be used for a broader range of environmental and aerosol conditions than these schemes, in general. Although the QDGE scheme mimics the parcel model well, it is also numerically efficient. Typically a parcel model simulation will take several minutes, while the QDGE scheme only consumes 0.1 seconds for the same case using a single core on Intel Xeon E5-2660 v2.

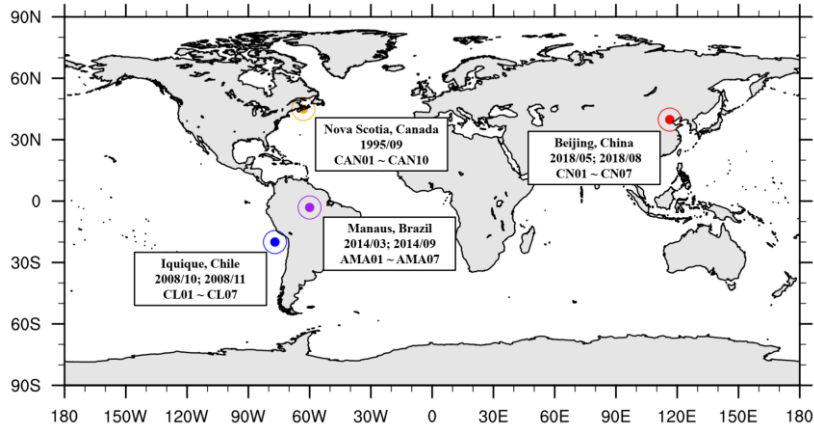
One more advantage of the QDGE scheme is the potential scale adaptivity for different vertical grids. The accuracy of the simulated supersaturation profile increases with the specified number of sub-levels (N_{sub}) and the number of iterations (I_{max}). Therefore, as the super-computer capabilities for climate model simulations are improved, the QDGE scheme will provide a more accurate solution for the activation process and easily adapts to the accuracy requirement for high-resolution GCMs in the future.

An earlier version of the QDGE scheme has been successfully used for simulations with the 5th generation of the Canadian atmospheric global climate model (CanAM5). It is currently being tested in additional models.

3 Data and methods

3.1 Campaign description

The worldwide cloud data used for the evaluation were sampled from four aircraft campaigns. The locations and instrument information of the four campaigns are shown in Fig. 4 and Table 2. The Canada (CAN) campaign provided marine stratus cloud data observed during the Radiation, Aerosol and Cloud Experiment (RACE) in Fall 1995 off the coast of Nova Scotia, Canada (Peng et al., 2002). The Chile (CL) campaign provided marine stratocumulus clouds data observed during the VAMOS Ocean-Cloud-Atmosphere-Land Study Regional Experiment (VOCALS-REx), for near-climatological atmospheric conditions off northern Chile and southern Peru (Wood et al., 2011). The Brazil (AMA) campaign provided continental stratus clouds data observed in Manaus, Brazil during the Green Ocean Amazon (GoAmazon2014/5) Experiment (Martin et al., 2016). The China (CN) campaign provided polluted continental stratus clouds data sampled in Beijing, China by the Beijing Weather Modification Office (Liu et al., 2020). These worldwide datasets comprise continental (CN and AMA), coastal (CAN), and marine (CL) meteorological conditions. Additionally, they cover different levels of human influence on clouds, with an observed range of the mean aerosol number concentration (N_a) within 100 m below the cloud base from 282 cm^{-3} to 1350 cm^{-3} .



235 **Figure 4.** The geographical distribution of 31 selected cloud cases in the four aircraft campaigns. The text boxes provide the locations, the periods, and the names of the cloud cases for each campaign.

Table 2. An overview of the four aircraft campaigns in this study.

Name	CAN	CL	AMA	CN
Date	1995/09	2008/10; 2008/11	2014/03; 2014/09	2018/05; 2018/08
Location	Nova Scotia, Canada	Iquique, Chile	Manaus, Brazil	Beijing, China
Cloud type	stratus	stratocumulus	stratus	stratus
Campaign name	RACE	VOCALS-REx	GoAmazon2014/5	/
CDNC instrument	FSSP (15 bins, 2.0~47.0 μm)	CAS (20 bins, 0.6~56.3 μm)	FCDP (20 bins, 1.5~150.0 μm)	FCDP (20 bins, 1.5~150.0 μm)
Aerosol instrument	PCASP (15 bins, 0.13~3.00 μm) ASAP (13 bins, 0.183~2.37 μm)	PCASP (30 bins, 0.09~3.00 μm)	PCASP (30 bins, 0.09~3.45 μm)	PCASP (30 bins, 0.10~3.00 μm)
Chemistry instrument	AMS	AMS	AMS	/
<i>LWC</i> instrument	King hot-wire probe	King hot-wire probe	King hot-wire probe and Johnson-Williams probe	King hot-wire probe
Atmospheric condition instrument	AIMMS	AIMMS	AIMMS	AIMMS
Number of selected cloud cases	10	7	7	7
Number of cases for w_c calculation	2	3	5	4
N_a	476	282 ± 116	846 ± 819	1350 ± 916

Note: N_a is the integrated number of particles detected by aerosol instruments and averaged within 100 m below the cloud base. The definition of cloud base and selection of cloud cases refer to Sect. 3.2.1. Calculation of w_c refers to Sect. 3.2.3.

240 Aerosol and cloud measuring instruments utilized in the four campaigns are briefly presented in Table 2. The observed variables mainly include the *CDNC*, the cloud liquid water content (*LWC*), the aerosol number-size distribution, the chemical

compositions of aerosol, and atmospheric condition parameters. For the measurement of the *CDNC*, the forward scattering spectrometer probe (FSSP) was used in the CAN campaign. The cloud, aerosol, and precipitation spectrometer (CAS) was used in the CL campaign. The fast cloud droplet probe (FCDP) was used in the AMA and CN campaigns. Although FCDP, FSSP, or CAS can observe cloud droplets with a particle size up to 150 μm , we only integrated the number for droplets with a particle size of 2 to 30 μm to derive the *CDNC*. Because cloud droplets larger than 30 μm are subject to collision-coalescence, and droplets smaller than 2 μm may be deactivated by evaporation (Fountoukis and Nenes, 2005). For the measurements of the *LWC*, the King hot-wire probe was used in all campaigns, and the Johnson-Williams probe was also equipped as an alternative option in GoAmazon2014/5. In terms of the aerosol observation, all the four campaigns utilized an onboard passive cavity aerosol spectrometer probe (PCASP), and some flights during the CAN campaign used the atmospheric solids analysis probe (ASAP), providing aerosol number concentration in multiple size bins roughly from 0.1 to 3 μm . We integrated the number for particles within the detected size range to determine N_a . In the CAN, AMA, and CL campaigns, the mass concentrations of aerosol chemical species, including NH_4^+ , NO_3^- , SO_4^{2-} , Cl^- , and organics (*org*), were measured using the aerodyne aerosol mass spectrometer (AMS). The CN campaign lacked data for aerosol chemical composition (see Sect. 3.2.2). For the CL campaign, five aircraft (i.e. Lockheed C-130, BAe-146, Gulfstream-1, Dornier-228, and Twin Otter) carried out observations (Wood et al., 2011). In order to ensure data integrity and consistency for aerosol number-size distribution and chemical composition measurements in the subsequent analysis, we only selected data from the Gulfstream-1 flights. The atmospheric condition parameters (T , pressure (P), relative humidity (RH), vertical velocity (w)) were mainly observed by the airborne integrated meteorological measurement system (AIMMS), in all campaigns. For the CL campaign, vertical velocity data were not available from the Gulfstream-1 flights, thus we used the observed w data from the Twin Otter flights that occurred simultaneous with Gulfstream-1 flights. Some meteorological variables that are required by the QDGE scheme, particularly including r_v , r_t , and h , were not available from the aircraft observations. Therefore, we calculated these based on other variables (Sect. 3.2.4). Detailed descriptions of the aforementioned observational instruments and data quality control procedures can be obtained from the relevant publications for the different aircraft campaigns (Li et al., 1998; Peng et al., 2002; Wood et al., 2011; Kleinman et al., 2012; Martin et al., 2016, 2017; Wang et al., 2020).

3.2 Data processing for closure experiment

3.2.1 Data extraction

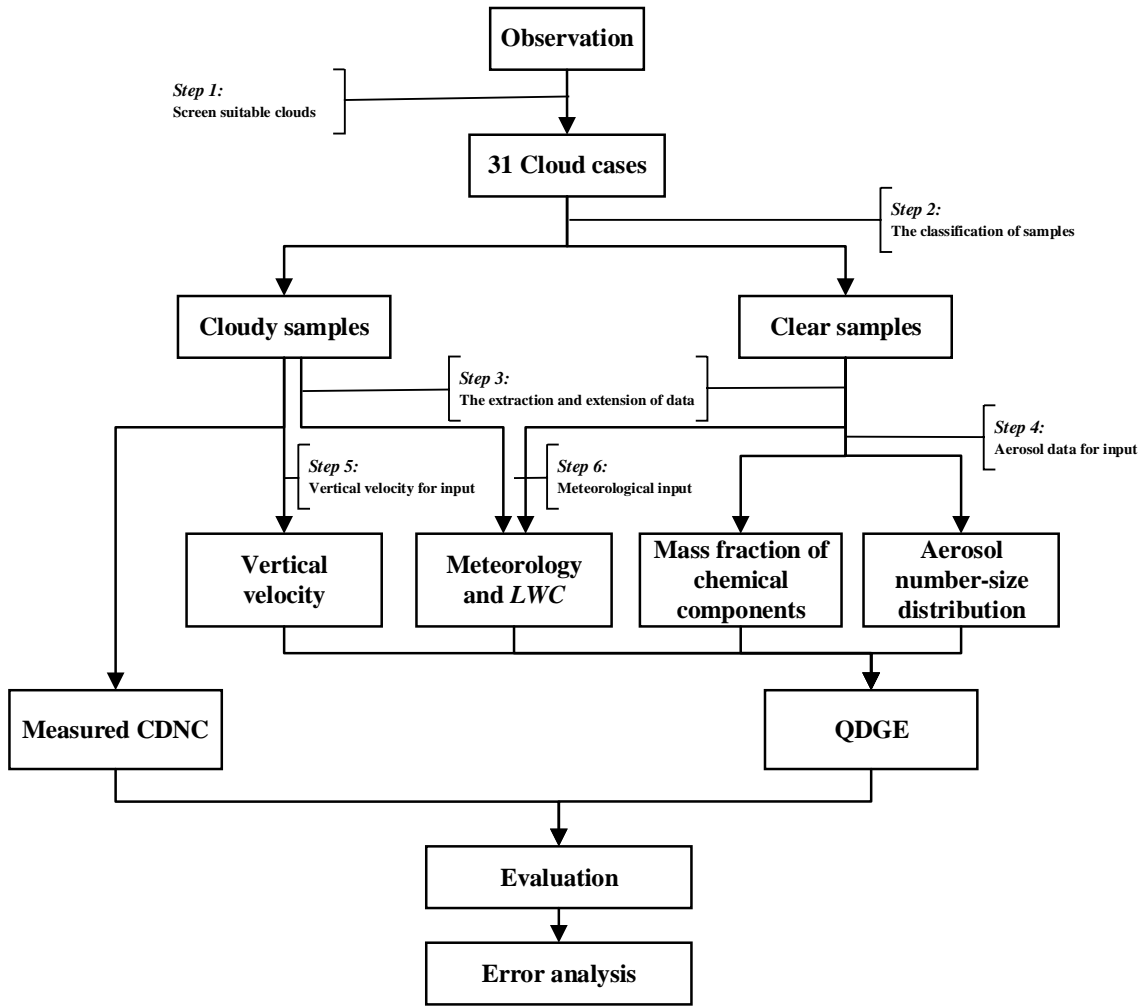
The flow chart of data extraction and processing is shown in Fig. 5. In the first step, we conducted a screening of observational data to obtain suitable cloud cases fulfilling the following conditions (Step 1 in Fig. 5). First, we selected cloud cases with continuous *LWC* profile with $T > 0$ $^\circ\text{C}$ and $LWC \geq 0.05$ g cm^{-3} in each layer, identifying the height of the cloud base as H_{low} (see Fig. B1). Second, we checked whether the *LWC* near the cloud base approximately satisfies the wet adiabatic assumption, that is, nearly free from entrainment. As shown in Fig. B1, we plotted the observed *LWC* and the

adiabatic LWC (LWC_{ad}) profiles, the later ones were calculated by assuming that LWC increases linearly with the height above cloud base (H_c), i.e. $LWC_{ad} = C_w H_c$. C_w is the adiabatic liquid water lapse rate, which is a function of temperature (Brenquier, 1991). For liquid clouds, the value of C_w varies from 0.5×10^{-3} to 3.0×10^{-3} g m^{-4} (Peng et al., 2002). For
 275 the cases shown in Fig. B1, C_w ranges from 0.6×10^{-3} to 2.8×10^{-3} g m^{-4} . The mean of C_w in each cloud case is shown in Table B2. Considering that the entrainment rate e was set to 1.0×10^{-3} m^{-1} (weak entrainment, Barahona and Nenes, (2007)) when running the QDGE scheme to be close to the real atmosphere, we identify the nearly adiabatic part in the cloud case (i.e. data sampled between H_{low} and H_{high} in Fig. B1) for obtaining the observed cloud properties for evaluating the simulation. Third, exclude the impact of collision-coalescence in the selected cloud cases, by ensuring that the water
 280 contents of cloud droplets with size greater than $30 \mu\text{m}$ were less than 0.05 g cm^{-3} . Finally, we checked to make sure each cloud case has N_a larger than $CDNC$. Ultimately, 31 eligible cloud cases were selected, as shown in Fig. B1. Table B2 listed the observed data in the selected cloud cases, $CDNC_0$ and LWC were averaged over the adiabatic part of each cloud case, N_a and RH were averaged within 100 m below the cloud base.

As shown in Step 2 of Fig. 5, we classified data samples of each cloud case into cloudy and clear conditions by utilizing the
 285 following criteria. Data sampled inside the cloud (cloudy condition) requires that $LWC \geq 0.05 \text{ g cm}^{-3}$, $CDNC > 10 \text{ cm}^{-3}$, and $RH \geq 99.5 \%$, and data samples outside the cloud (clear condition) requires that $LWC < 0.05 \text{ g cm}^{-3}$, $N_a > 10 \text{ cm}^{-3}$, and $RH < 99.5 \%$.

During each flight, the sampling along the horizontal flight track was continuous, which allowed us to better characterize the cloudy conditions or atmospheric conditions inside or outside the cloud. In all the 31 selected cloud cases, we were able to
 290 extract data samples at nl levels ($l_d, d = 1, 2, \dots, nl$ from the cloud base; where nl is usually 4, at least 2.) along horizontal flight tracks in each cloud case, and calculated the mean value of the observed variable v (V_{v,l_d}) along the horizontal track in each level l_d . V_{v,l_d} is then extended to the vertical model levels ($L_f, f = 1, 2, \dots, NL$; where L_f refers to the interfaces of the vertical layers in the model, i.e. $\Delta z = L_{f+1} - L_f$) for running the QDGE scheme, which is Step 3 as shown in Fig. 5. The extension proceeded with the following rules: The meteorological variables profile in clear condition, such as T , P , and r_t ,
 295 were extended downwards to the surface by using hydrostatic equation and ideal gas law, then extended to the top by linear extrapolation, and interpolated between l_1 and l_{nl} . The aerosol mass and number profiles were extended to surface and top by linear extrapolation and interpolated between l_1 and l_{nl} . RH was filled between l_1 and l_{nl} by linear interpolation.

For each cloud case, the data samples in the clear air were used to obtain aerosol-related input information for the model simulations (number and mass concentrations of aerosol components in different particle size sections) and the profiles of
 300 meteorological parameters. The data samples in cloudy conditions were used to obtain the vertical velocity and LWC as input for the model, and to provide measured $CDNC$ for comparisons with model results and closure verification. Here, LWC of the host model was converted into q_w to calculate the initial r_t and h in the QDGE scheme (Fig. 2 and Eqs. 8-12). These are Steps 4, 5, and 6, as shown in Fig. 5 and described in the next three subsections.



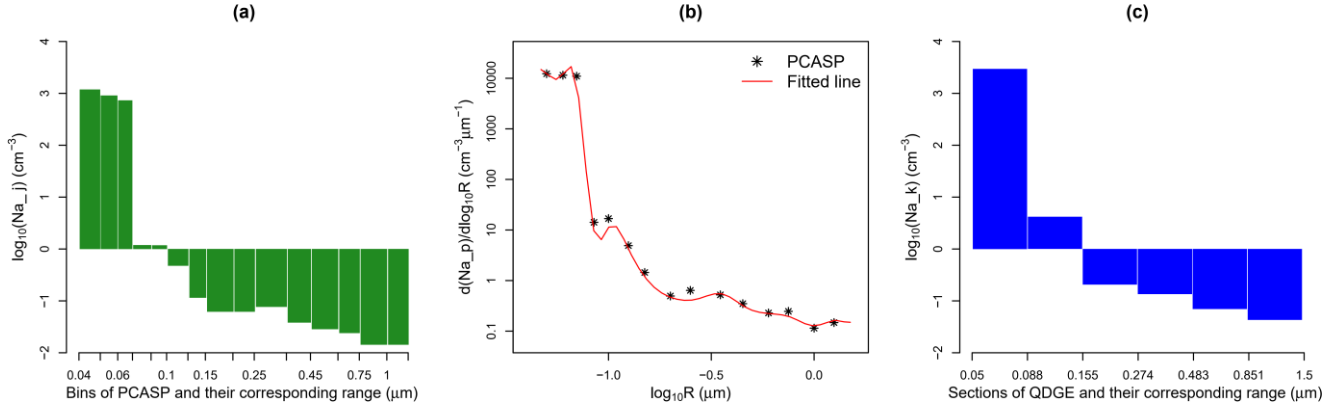
305 **Figure 5. A flow chart to schematically show the data extraction and processing for this work.**

3.2.2 Aerosol data for input

In each of the cloud cases from the different aircraft campaigns, aerosol number concentrations $N_{a,j}$ ($j = 1, \dots, nj$; where nj is the number of size bins detected in observation, see Table 2) sampled by ASAP or PCASP were categorized in 13, 15, or 30 bins. The size-resolved aerosol number concentrations were subsequently interpolated to a common particle size distribution (PSD) with 6 prescribed size sections for model input based on the following method (as depicted in Fig. 6).
 310 First, we used the aerosol number concentration in each size bin of the PCASP (or ASAP) data to fit a continuous PSD using cubic spline interpolation (Fig. 6b). Second, we integrated the fitted PSD to obtain the aerosol number concentration $N_{a,k}$ ($k=1, \dots, 6$) in the aerosol size sections employed by the QDGE scheme (the dry aerosol particle radius boundaries are at 0.050, 0.088, 0.155, 0.274, 0.483, 0.851, 1.500 μm , as shown in Fig. 6c). By utilizing this method, the total N_a obtained by

315 integration over the 6 QDGE sections was slightly different from the observed total aerosol number due to the fitting of PSD, thus we further weighed the total fitted aerosol number concentration by the observed aerosol number to ensure the conservation of total number concentration (i.e., the total N_a integrated over the QDGE sections in Fig. 6c is the same as the aerosol number integrated over the observed PSD in Fig. 6a). Finally, the PSD of the aerosol number concentration in 6 sections (Fig. 6c) was used as input to the QDGE scheme.

320



325 **Figure 6.** The processing of the observed aerosol number-size distribution for the input to the QDGE scheme. (a) the observed aerosol number concentration in each size bin sampled by PCASP, (b) the particle size distribution curve (red line) fitted to the observations (the asterisks refer to the observations that were derived from (a)), and (c) aerosol number concentration in 6 size sections, as prescribed in model simulations with the QDGE scheme.

For each of the CAN, AMA, and CL campaigns, the AMS provided measurements of chemical components over the entire campaign, providing concentrations of NH_4^+ , NO_3^- , SO_4^{2-} , Cl^- , and *org*. The various chemical components in the aerosol were assumed to be internally mixed, thus all aerosol particles with the same size have the same composition. To obtain the PSD of mass concentration of each chemical component, we made use of the AMS measurements. For continental campaigns such as CN and AMA, we assumed that aerosols are composed of NH_4NO_3 , $(NH_4)_2SO_4$, NH_4Cl , and organics (*Org*) (Shilling et al., 2018; Zhou et al., 2019; Li et al., 2020). For coastal or oceanic campaigns such as CAN and CL, we took sea salt (*NaCl*) into account, too. For the CAN, AMA, and CL campaigns, we converted the AMS data of ion mass (AMS_{ci} , ci is NO_3^- , SO_4^{2-} , Cl^- , or *org*) to the mass of each chemical component (m_c , c is NH_4NO_3 , $(NH_4)_2SO_4$, NH_4Cl , organics (*Org*), or *NaCl*).

335
$$m_{NH_4NO_3} = \frac{AMS_{NO_3^-}}{M_{NO_3^-}} M_{NH_4NO_3}, \quad (15)$$

$$m_{(NH_4)_2SO_4} = \frac{AMS_{SO_4^{2-}}}{M_{SO_4^{2-}}} M_{(NH_4)_2SO_4}, \quad (16)$$

$$m_{NH_4Cl} = \frac{(1-\alpha)AMS_{Cl^-}}{M_{Cl^-}} M_{NH_4Cl}, \quad (17)$$

$$m_{NaCl} = \frac{\alpha AMS_{Cl^-}}{M_{Cl^-}} M_{NaCl}, \quad (18)$$

$$m_{Org} = AMS_{Org}, \quad (19)$$

340 where M_{ci} and M_c are the molecular weight of ion ci and chemical component c , respectively. Here we assume that concentrations of NH_4^+ are sufficiently high to balance all anions. The mass of sea salt in different campaigns is controlled by a given factor α to partition the amount of Cl^- in sea salt and continental chemical components. We set the values of α as 0, 90%, and 95% for AMA, CAN, and CL campaigns. That is, 90% and 95% of Cl^- are attributed to sea salt in the coastal campaign CAN and the oceanic campaign CL, respectively. Based on the calculated mass concentration of each chemical

345 component, the average density of aerosol can be obtained:

$$\rho_a = \frac{\sum_{c=1}^5 m_c}{\sum_{c=1}^5 m_c / \rho_c}, \quad (20)$$

where ρ_c is the density of each component c , and they are 1725, 1769, 1527, 1900, and 1400 $kg\ m^{-3}$ for NH_4NO_3 , $(NH_4)_2SO_4$, NH_4Cl , $NaCl$, and Org , respectively (Ferek et al., 1998; Nakao et al., 2013). Consequently, we can obtain the mass concentration (unit $kg\ cm^{-3}$) of each component c in section k following this equation:

$$350\ Mass_{c,k} = \frac{m_c}{\sum_{c=1}^5 m_c} \cdot N_{a,k} \frac{4\pi}{3} R_k^3 \rho_a, \quad (21)$$

where R_k is the median radius of section k .

Since no AMS data are available for the CN campaign, we assumed the mass fraction of different chemical components according to contemporaneous measurements in Beijing, China (Zhou et al., 2019; Li et al., 2020), as shown in Table B3.

Under the assumption of $\rho_a = 1600\ kg\ m^{-3}$ (Levy Zamora et al., 2019), $Mass_{c,k}$ in the CN campaign can be obtained from

355 Eq. (21).

Finally, we obtained the number concentration of total aerosol and the mass concentration of each chemical component from PCASP/ASAP and AMS measurements in each cloud case and calculated aerosol number and mass concentrations in 6 prescribed size sections following the above procedures (Step 4 in Fig. 5). We then used the aerosol information as input to drive the QDGE scheme.

360 3.2.3 Vertical velocity for input

The averaged updraft velocity (w_+) and sub-grid vertical velocity (w_{sub}) obtained from the observed vertical velocity (w) samples in clouds were used to calculate w_c ($w_c = w_+ + w_{sub}$) as input for running the QDGE scheme (Step 5 in Fig. 5). The updraft velocity is a key variable for parameterizing aerosol activation. Peng et al. (2005) pointed out that using a characteristic value of the vertical velocity distribution (0.8 times the standard deviation of the distribution) is a good

365 approximation for simulating the nucleated cloud droplet number of marine stratus when running the parcel model. Meskhidze et al. (2005) also gave a method to calculate w_+ , which had the optimal closure for cumulus and stratocumulus clouds. Here, we derived a universal method for calculating w_+ in stratus and stratocumulus based on the above two studies.

According to Meskhidze et al. (2005), the averaged updraft velocity (w_+) can be calculated by probability density function (PDF) of w , $p(w)$:

$$370 \quad w_+ = \frac{\int_0^\infty wp(w)dw}{\int_0^\infty p(w)dw}. \quad (22)$$

For the normal PDF with the mean velocity w_0 and standard deviation σ , $p(w)$ can be represented as

$$p(w) = \frac{1}{\sqrt{2\pi}\sigma} \exp\left(-\frac{(w-w_0)^2}{2\sigma^2}\right) = \beta\phi(\omega), \quad (23)$$

where $\omega = \beta w + \gamma$, $\beta = 1/\sigma$, $\gamma = -w_0/\sigma$, and $\phi(\omega)$ is the standard normal PDF.

Use Eq. (23) into Eq. (22) we obtain

$$375 \quad w_+ = \frac{\Phi(\gamma)}{(1-\Phi(\gamma))\beta} - \frac{\gamma}{\beta} = \frac{\Phi(\gamma)}{(1-\Phi(\gamma))} \sigma + w_0, \quad (24)$$

where $\Phi(\gamma)$ is the cumulative distribution function of the standard normal PDF that can be represented by error function (erf):

$$\Phi(\gamma) = \int_{-\infty}^{\gamma} \phi(t)dt = \frac{1}{2} \left(1 + \operatorname{erf}\left(\frac{\gamma}{\sqrt{2}}\right)\right). \quad (25)$$

Especially, when $w_0 = 0$,

$$380 \quad w_+ = \frac{\Phi(0)}{(1-\Phi(0))} \sigma = \sqrt{\frac{2}{\pi}} \sigma \cong 0.8\sigma, \quad (26)$$

which is consistent with the characteristic velocity pointed by Peng et al. (2005) used for assessing cloud droplet closure for stratocumulus clouds sampled in the CAN campaign.

A sub-grid vertical velocity (w_{sub}) is needed for the QDGE scheme, and it can be derived from the square root of the Turbulent Kinetic Energy (TKE) following Morrison and Pinto (2005):

$$385 \quad w_{sub} = \sqrt{\frac{2}{3} TKE}, \quad (27)$$

where the TKE is given by

$$TKE = \frac{1}{2} (\overline{(u')^2} + \overline{(v')^2} + \overline{(w')^2}), \quad (28)$$

In this study, we assume that no horizontal movement occurs in cloud during the horizontal flight tracks, that is, $\overline{(u')^2} = \overline{(v')^2} = 0$ and $\overline{(w')^2} = \sigma^2$. Therefore, the sub-grid vertical velocity can be represented by σ :

$$390 \quad w_{sub} = \frac{\sigma}{\sqrt{3}}. \quad (29)$$

If the observed w in each selected cloud case obeyed the normal distribution, we could calculate w_c ($w_c = w_+ + w_{sub}$) following Eqs. (24) and (29) as input for running the QDGE scheme easily. We checked the normality of w distribution by drawing a quantile-quantile (Q-Q) plot using the observed w values along the horizontal flight track of the cloud case, taking CN01 as an example in Fig. 7. The linearity between the Q-Q plot of observed w samples and a standard normal distribution

395 indicates that w data does indeed follow the normal distribution.

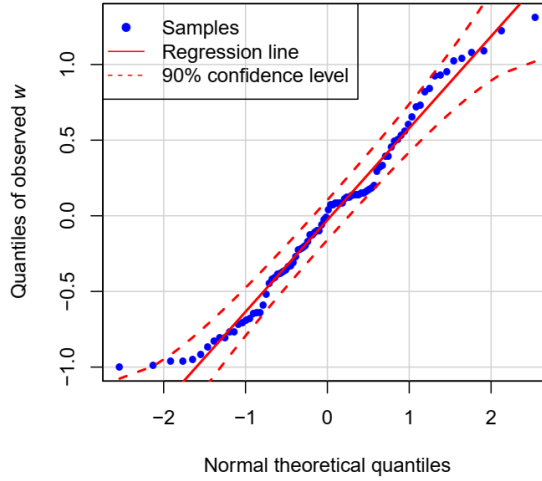


Figure 7. A normal quantile-quantile plot for comparing the observed w sampled by aircraft in cloud case CN01 with a standard normal distribution. The linearity of the data points (blue) suggests that the observed w are normally distributed.

In the four campaigns of this study, 4 cloud cases in CN, 2 cases in CAN, 5 cases in AMA, and 3 cases in CL have enough data samples to obtain the PDF of w (Table 2), as plotted for checking the normality of w distribution in Fig. B2. However, the w PDF in two of the CAN cloud cases does not conform to the normal distribution very well (panel (5) and (6) of Fig. B2). So, we used the mean and standard deviation of w distribution in Peng et al. (2005) to obtain w_c in the CAN campaign. For the CN, AMA, and CL campaigns, we directly calculated the w_c from available data samples for the cloud cases plotted in Fig. B2 and used their mean values for cloud cases lacking enough w values in each campaign (Table B2).

3.2.4 Meteorological input

Some meteorological variables (T , P , RH , and LWC) can be obtained from AIMMS measurements directly, though, others (r_v , r_t , and h) need to be calculated according to available variables (Step 6 in Fig. 5). We obtained r_v by the following equation:

$$r_v = \frac{\varepsilon e_* RH}{P - e_* RH}, \quad (30)$$

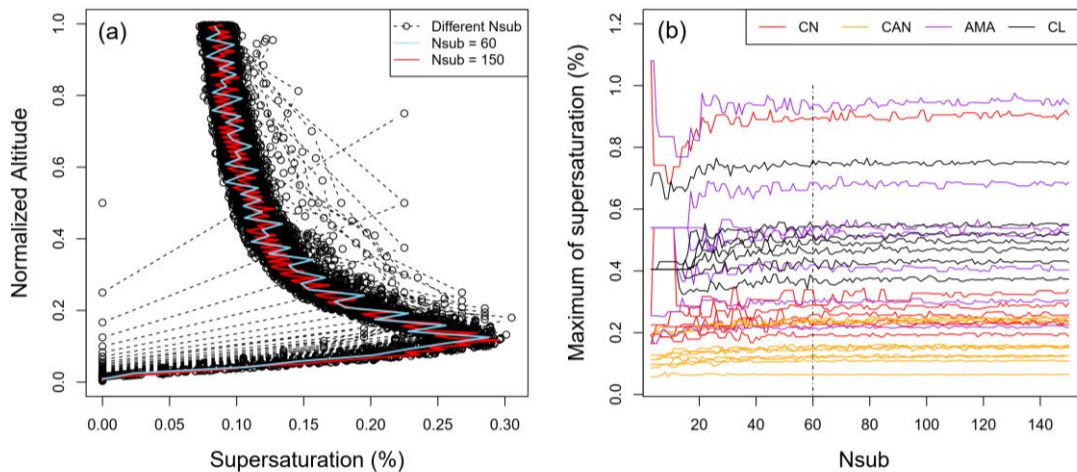
where e_* can be estimated by referring to Murray (1967):

$$e_* = 6.1078e^{\left(\frac{17.2694(T-273.16)}{T-35.86}\right)}. \quad (31)$$

Then, r_t and h can be obtained by Eqs. (8) and (9) from r_v and other available variables. All meteorological variables were extracted and interpolated to model levels, as described in Sect. 3.2.1. The profiles of measured meteorological variables served as the initial state to drive the QDGE scheme.

As mentioned in Sect. 2.1, the QDGE scheme simulates vertical profiles of supersaturation to determine S_{max} , for a vertical grid with the size $\Delta z_s = \Delta z / N_{sub}$, where Δz is the grid size of the atmospheric host model. The accuracy of the simulated supersaturation profile generally increases with N_{sub} , though, large values of N_{sub} imply higher computational burdens. For applications of the QDGE scheme in atmospheric models, it is therefore important to determine an optimal value of N_{sub} that yields sufficiently accurate supersaturation profiles at acceptable costs.

Figure 8a plots the vertical profiles of S simulated by the QDGE scheme with different N_{sub} values for the cloud case CN01. The results show that each profile with $N_{sub} \geq 3$ produces a well-defined maximum of S (S_{max}), which approaches to a stable value as N_{sub} is further increased. All cases seem to converge to a similar value as S_{max} with $N_{sub} = 150$, as plotted in Fig. 8a. Figure 8b shows the variation of S_{max} with the increasing N_{sub} for all cloud cases in the four campaigns. Overall, S_{max} fluctuates dramatically with $N_{sub} < 10$, but plateaus when N_{sub} is greater than 60 (10 for CAN). Results obtained for $N_{sub} = 150$ and $N_{sub} = 60$ are similar. The mean relative error and correlation coefficient between S_{max} with $N_{sub} = 150$ and that with $N_{sub} = 60$ are 1.97% and 0.9997, respectively. Therefore, we used $N_{sub} = 60$ in this study ($N_{sub} = 10$ for CAN). Further discussion regarding the selection of N_{sub} are provided in Sect. 5.



430 **Figure 8. (a) Vertical profiles of the simulated supersaturation for different N_{sub} (1-150) in the QDGE scheme for the cloud case CN01. (b) Changes of the maximum supersaturation with different N_{sub} for all cloud cases in the four campaigns.**

3.3 Statistical parameters for evaluation and error analysis

The QDGE scheme simulates the $CDNC$ ($CDNC_M$) in each cloud case, based on S_{max} . Noting that $CDNC_M$ is not exactly the same as N_{CCN} here, as we take wet particles with a size between 2 to 30 μm to compare with the observed one. Considering that aerosol activation is particularly efficient in the vicinity of the cloud base in stratus and convective clouds, the QDGE

scheme only calculates the $CDNC$ at the cloud base (Sect. 2.1). Here, we considered the effect of weak entrainment on the vertical profile of the cloud droplet number mixing ratio to be close to the real cloud base in the atmosphere (Sect. 3.2.1). Therefore, we evaluated the performance of the QDGE scheme by comparing $CDNC_M$ with the vertically average value of the observed $CDNC$ ($CDNC_O$) in the nearly adiabatic part of the cloud (between H_{low} and H_{high} in Fig. B1) (Sect. 3.2.1),

440 given by

$$CDNC_O = \frac{1}{N_O} \sum_{H=H_{low}}^{H_{high}} CDNC_{O,H}, \quad (32)$$

where N_O is the number of samples between H_{low} and H_{high} , and $CDNC_{O,H}$ is the observed $CDNC$ in height H .

Correspondingly, the mean relative error (MRE) of each cloud case can be calculated, as follows:

$$MRE = \left| \frac{CDNC_M - CDNC_O}{CDNC_O} \cdot 100\% \right|, \quad (33)$$

445 where MRE of each cloud case will also be used for subsequent error analysis.

To evaluate the overall accuracy of the QDGE scheme, we also calculated the mean values of $CDNC_O$, $CDNC_M$, MRE for cloud cases in each campaign, namely $\overline{CDNC_O}$, $\overline{CDNC_M}$, and \overline{MRE} . Besides, the R^2 (R is the Pearson correlation coefficient) between the $CDNC_O$ and $CDNC_M$ in each campaign was also calculated.

To quantify the contributions of different physical variables to errors in the simulated $CDNC$ with the QDGE scheme, we
 450 calculated the Maximum Information Coefficient (MIC) (Reshef et al., 2011), which provides a measure for the strength of the relationship between each input variable and MRE . MIC can be a good measure to capture the association between the attributive variable and MRE for different types of relationships, such as linear, exponential and many complex functional relationships (Reshef et al., 2011). There is no need to standardize the data before the MIC calculation and the calculations have low computational complexity and high robustness. However, it should be noted that the association here does not refer
 455 to a specific correlation, such as temporal or spatial correlation, or positive or negative correlation, but refers to the strength of a certain relationship between the variable and MRE . The MIC value is always between 0 and 1. The higher the MIC value, the stronger the association between the input variable and MRE , that is, the input variable contributes more significantly to the MRE . Here, we calculated the MIC base on the minepy package in Python (Albanese et al., 2018), and set the parameters required in MIC as the default settings suggested by the code developers. Different parameters had an
 460 insignificant effect on the relative importance of variables and MRE .

We calculated the MIC between MRE and each one of the following input variables: the relative humidity (RH), the mean vertical velocity (w_+) and the sub-grid vertical velocity (w_{sub}) to represent environmental and dynamic conditions; the total aerosol number (N_a) as a proxy of pollution level; the hygroscopicity of aerosol (K_m) weighted by composition volume fraction, and the effective radius of aerosol PSD ($R_{e,a}$) to represent the chemical and size properties of the aerosol. Here, K_m ,

465 and $R_{e,a}$ are defined as:

$$K_m = \frac{\sum_{c=1}^5 \frac{m_c \kappa_c}{\rho_c}}{\sum_{c=1}^5 \frac{\bar{m}_c}{\rho_c}}, \quad (34)$$

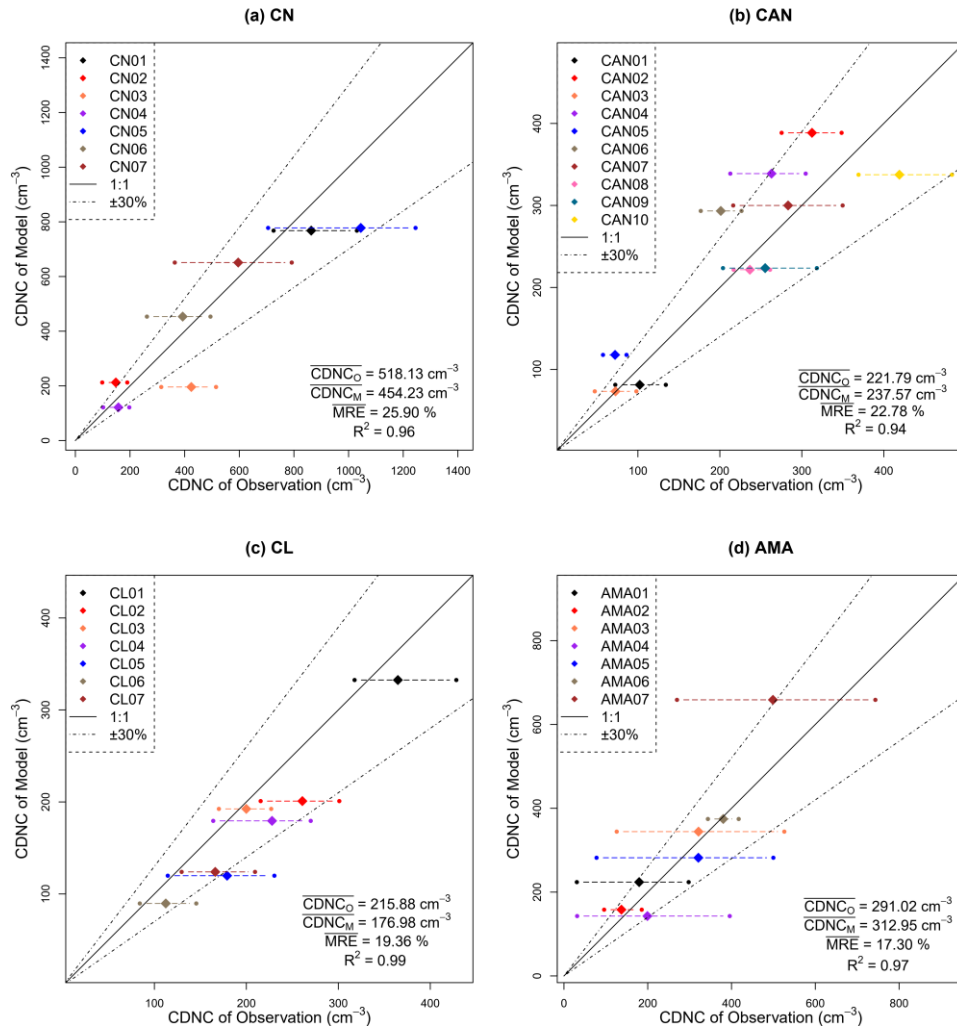
$$R_{e,a} = \frac{\sum_{j=1}^{n_j} R_j^3 N_{a,j}}{\sum_{j=1}^{n_j} R_j^2 N_{a,j}}, \quad (35)$$

where κ_c , the hygroscopicity of component c , is accounted for variations with relative humidity in the QDGE scheme (Appendix A). R_j represents the middle radius in the j^{th} particle size bin observed by PCASP or ASAP (see Sect. 3.2.2 and Table 2). For MIC calculation, the values of input variables derived from observations are listed in Table B2 for each cloud case.

4 Results

4.1 Closure experiment

The results of the closure experiment are shown in Fig. 9. Almost all $CDNC_M$ values fall within 30 % of the mean observations in the clouds. R^2 is above 0.94 for all campaigns, which indicates a good agreement between simulation and observation. For the four campaigns covering marine to continental conditions, the \overline{MRE} values are all below 26 %. The AMA campaign produces the best agreement between model results and observations, with a \overline{MRE} value of 17.30 %. On the other hand, the CN campaign produces a poor agreement, with a \overline{MRE} value of 25.90 %. However, cloud droplet number concentrations are underestimated for all cloud cases for the CL campaign (Fig. 9c), which may be related to the high activation ratio (AR , the ratio of N_a to $CDNC_O$, see Table B2) in this region. AR in all CL cases are higher than 60 %, suggesting that the marine environment is favorable for more aerosol particles to be activated. If particles with a smaller size than the detection limit of PCASP (about 10 nm) are activated, it could lead to an underestimation of the simulated $CDNC$ in the CL campaign.



485 **Figure 9. A closure experiment between CDNC_O and CDNC_M for each cloud case in the (a) CN, (b) CAN, (c) CL, and (d) AMA campaigns. The horizontal dashed lines represent the range of the observed CDNC within the 25% and 75% quantiles.**

In order to provide further context, we compare the $\overline{\text{MRE}}$ values of this study to previous studies with different aerosol activation parameterizations and aircraft measurements, as shown in Table 3. The $\overline{\text{MRE}}$ values are relatively high for those early parameterizations, basically around 50 %. In the recent two decades, the performance of physically-based
 490 parameterization has been significantly improved, as is evident from a reduction of the $\overline{\text{MRE}}$ to about 30 %. For instance, one of the schemes (Fountoukis and Nenes, 2005) achieved remarkable closure (with $\overline{\text{MRE}}$ of 13.5 %) for continental cumuliform/stratus. In this study, the QDGE scheme performs decently (the $\overline{\text{MRE}}$ values are all below 26 %) in four different regions, indicating that the scheme is suitable for simulations of cloud droplet number concentrations over a wide range of different meteorological conditions and different levels of aerosol pollution.

495 **Table 3. Comparison of results from simulations with activation schemes and the QDGE method (Mainly referring to Fountoukis et al. (2007))**

Parameterization or Model	\overline{MRE} (%)	Observed cloud type	Location	Reference
Flossmann et al. (1985)	~50.00	Continental stratocumulus	North of England	(Hallberg et al., 1997)
UWyo parcel model	<50.00	Marine stratocumulus	Tenerife, Spain	(Snider et al., 2003; Snider and Brenguier, 2000)
Fountoukis and Nenes (2005); Nenes and Seinfeld (2003)	~30.00	Coastal stratus	Monterey, California, USA	(Meskhidze et al., 2005)
Fountoukis and Nenes (2005)	13.50	Continental cumuliform /stratus	Cleveland and Detroit, USA	(Fountoukis et al., 2007)
Kivekäs et al. (2008)	~35.00	Continental stratus	North of Finland	(Kivekäs et al., 2008)
	17.30	Continental stratus	Manaus, Brazil	
	19.36	Marine stratocumulus	Iquique, Chile	
QDGE scheme	22.78	Costal stratus	Nova Scotia, Canada	This work
	25.90	Continental stratus	Beijing, China	

4.2 Error analysis

Although the performance of the QDGE scheme is good in different aircraft campaigns, it is useful to analyze sources of biases in the simulations. Following the procedures described in Sect. 3.3, we calculated the Maximum Information Coefficient (MIC) between MRE and the input variables of the QDGE scheme, including aerosol properties (K_m , and $R_{e,a}$), thermodynamic state (RH), pollution level (N_a), and atmosphere dynamic conditions (w_+ and w_{sub}), as shown in Table B2. The MIC values for all cloud cases and each campaign have been shown in Table 4.

For almost all campaigns, the aerosol number concentration and the hygroscopicity, have the most significant impacts on MRE . This is consistent with the change of environmental supersaturation (Eq. (3)), according to which the variation of supersaturation S with height is essentially determined by the competition between the production of S by adiabatic cooling and the reduction in S from condensational growth of the particles, the latter mainly depends on the number and solubility of the aerosol particles. In detail, N_a has a greater impact on MRE in marine regions (CAN and CL), but K_m is more significant in continental regions (CN and AMA). In marine regions, where N_a is relatively low (Table 2), a small fluctuation in N_a can cause noticeable changes in the simulated S_{max} and CDNC, which makes MRE more sensitive to N_a . However, in continental areas, N_a is relatively high, and the change in hygroscopicity becomes more important to MRE . The atmospheric humidity and the dry size of the aerosol particle also have non-negligible impacts on MRE . Both affect the hygroscopic growth of aerosol particles and the reduction in S . Overall, the atmosphere dynamic conditions have the most insignificant impact on MRE , which may be attributed to the weak variation of them in stratus and stratocumulus clouds (Table B2).

The MIC values also help to explain the relatively poor simulation performance of some campaigns. The chemical properties of the aerosol, which affect K_m , are very important for the simulation in the continental region, but the CN campaign lacks AMS data and we applied the same chemical composition for all cloud cases, based on earlier measurements in this region (Sect. 3.2.2). Given the importance of the chemical properties, simultaneous measurements of chemical components probably would have helped to enhance the accuracy of simulated $CDNC$ for the CN campaign. Another possible cause of biases in simulated $CDNC$ for the CN campaign is a much larger standard deviation of observed N_a (see Table 2) than that of other campaigns, which could be responsible for the error in the simulated $CDNC$. However, it should be noted that although the CAN campaign is characterized by the presence of coastal clouds and smaller variations in N_a , its MRE is higher than the AMA campaign, which may be related to the application of uniform updraft velocity in simulations for the CAN campaign (Sect. 3.2.3 and Table B2).

Overall speaking, the errors in the simulated $CDNC$ is largely relevant to the missing data in observation (such as CN and CAM campaign), the analysis of MIC and error sources here could provide a good reason to develop and improve measurement strategies in the future aircraft campaigns.

Table 4. The calculated MIC values between MRE and different input variables for all cloud cases and each campaign.

	CN	CAN	CL	AMA	ALL
K_m	0.522	N_a 0.610	RH 0.522	K_m 0.522	N_a 0.343
RH	0.522	K_m 0.396	N_a 0.470	N_a 0.522	K_m 0.315
N_a	0.470	$R_{e,a}$ 0.396	K_m 0.292	w_+ 0.470	RH 0.242
w_+	0.470	RH 0.396	$R_{e,a}$ 0.198	w_{sub} 0.470	$R_{e,a}$ 0.202
w_{sub}	0.470	w_+ 0.000	w_+ 0.198	RH 0.292	w_+ 0.170
$R_{e,a}$	0.292	w_{sub} 0.000	w_{sub} 0.198	$R_{e,a}$ 0.198	w_{sub} 0.170

5 Conclusions and discussion

In this paper, we introduce a numerically efficient aerosol activation scheme, which calculates the maximum cloud supersaturation and cloud droplet number concentration ($CDNC$) by employing a Quasi-steady state approximation of the cloud Droplet Growth Equation (QDGE) scheme. The QDGE scheme utilizes the look-up table and iterative calculation for solving the sub-level variation of supersaturation and deriving the maximum supersaturation and the activated particle number-size distribution in the large-scale grid of climate models. The comparison between the results of the QDGE scheme and a parcel model shows that biases in the maximum supersaturation under different environmental and aerosol conditions are within 0.18 % (with an average of 0.05 %), consistent with the high accuracy of the QDGE scheme. Whereafter, we evaluated the simulated $CDNC$ with worldwide cloud data sampled during four aircraft campaigns, covering a wide range of different meteorological conditions and different levels of aerosol pollution. The aerosol information, updraft velocity, and meteorological conditions were carefully extracted from aircraft measurements and applied to drive the QDGE scheme. The simulated $CDNC$ is compared with the observed correspondence in the nearly adiabatic part of the cloud, for evaluating the

540 performance of the scheme. The average values of the mean relative error in the four campaigns are all within 26%, indicating that the QDGE scheme can reasonably simulate the activated *CDNC* on a regional or global scale. We also investigated the potential sources of error in the simulated *CDNC* and found that the magnitude of the mean relative error is mostly relevant to the aerosol number concentration in marine regions and to aerosol hygroscopicity in continental regions than to other variables in the simulation.

545 Several points are worthy of mentioning for future work. The QDGE scheme can be further optimized in several aspects. First, $N_{sub} = 60$ generates reasonably good results in four different regions in this study, but this number is a little high and the computation will be too demanding to apply in general circulation models. Second, the iterative calculation to derive supersaturation in each sub-grid level can be computationally expensive. Therefore, both adjustments on N_{sub} number and optimization on the iteration would be necessary before the QDGE scheme is applied in the climate model. These works
550 would be considered in future studies.

Appendix A: Parameters

The parameters A , B , C , D , and E in Eqs. (1-3) are given by

$$A = \frac{2M_w\sigma}{RT\rho_w}, \quad (A1)$$

$$B = \kappa R_p^3, \quad (A2)$$

$$555 \quad C = \frac{\rho_w RT}{e_* D'_v M_w} + \frac{L_v \rho_w}{K'_a T} \left(\frac{L_v M_w}{RT} - 1 \right), \quad (A3)$$

$$D = \frac{g M_w L_v}{c_p R T^2} - \frac{g M_a}{RT}, \quad (A4)$$

$$E = \frac{P M_a}{e_* M_w} + \frac{M_w L_v^2}{c_p R T^2}, \quad (A5)$$

where κ is the aerosol hygroscopicity, σ is the surface tension of the solution/air interface (which is approximated by the surface tension of water here), ρ_w is the density of water, M_w is the molecular weight of water, R is the universal gas
560 constant, T is the temperature, R_p is the dry aerosol particle radius, e_* is the saturation vapor pressure, L_v is the latent heat of vaporization, K'_a is the modified thermal conductivity of air accounting for non-continuum effects, D'_v is the modified diffusivity of water vapor in air accounting for non-continuum effects (Seinfeld and Pandis, 2016), g is the gravitational constant, M_a is the molecular weight of dry air, P is the atmospheric pressure, and c_p is the heat capacity at a constant pressure of dry air.

565 Petters and Kreidenweis (2007) proposed a parameter κ for representing the hygroscopicity of aerosol with a variety of chemical compounds, and provided tabulated values of κ based on laboratory data and modeling. They found that the aerosol water content (the ratio of wet aerosol volume to the dry aerosol volume) parameterized on κ was generally within the experimental uncertainty, but biased at low relative humidity (Kreidenweis et al., 2008; Petters and Kreidenweis, 2007).

570 Kreidenweis et al. (2008) evaluated the calculated aerosol water content based on κ with the Aerosol Inorganic Model (AIM; Wexler and Clegg (2002)), which gives evidence for systematically different results at low aerosol water contents for some compounds. In order to improve biases at low relative humidity, the original method was extended to account for variations in κ with relative humidity in the QDGE scheme. Specifically, piecewise-linear relationships between κ and aerosol water activity for different chemical components were determined based on results from AIM.

Appendix B: Tables and Figures

575 **Table B1. Aerosol distribution and property parameters, referring to Whitby (1978) and Ghan et al. (2011).**

Aerosol type	Mode number concentration (cm^{-3})	Mode radius (μm)	Mode geometric standard deviation	κ	e	Condensation coefficient
Marine	340, 60, 3.1	0.005, 0.035, 0.31	1.6, 2.0, 2.7			
Clean continental	1000,800,0.72	0.008, 0.034, 0.46	1.6, 2.1, 2.2	0.7	0	1
Background	6400,2300,3.2	0.008, 0.038, 0.51	1.7, 2.0, 2.16			
Urban	106000,32000,5.4	0.007, 0.027, 0.43	1.8, 2.16, 2.21			

Table B2. A summary of observed ($CDNC_O$, N_a , RH , and LWC), derived (AR , Sol , C_w , K_m , $R_{e,a}$, w_+ , and w_{sub}), simulated and evaluative ($CDNC_M$ and MRE) variables of each cloud case in four campaigns.

Case	Observed variables				Derived variables								Simulated and evaluative variables	
	$CDNC_O$ (cm^{-3})	N_a (cm^{-3})	RH (%)	LWC (g cm^{-3})	AR (%)	Sol (%)	C_w (10^{-3} g cm^{-4})	K_m	$R_{e,a}$ (μm)	w_+ (m s^{-1})	w_{sub} (m s^{-1})	$CDNC_M$ (cm^{-3})	MRE (%)	
CN01	863.25	3016.27	67.92	0.20	28.62	65.00	0.69	0.37	0.23	0.469	0.340	767.86	11.05	
CN02	148.17	372.77	61.89	0.06	39.75	65.00	0.71	0.39	0.41	0.609	0.441	212.3	43.28	
CN03	424.41	432.05	61.89	0.08	98.23	65.00	1.04	0.39	0.15	0.609	0.441	195.84	53.86	
CN04	157.49	1738.09	57.71	0.12	9.06	65.00	0.81	0.40	0.98	0.609	0.441	121.33	22.96	
CN05	1044.72	1550.93	88.12	0.43	67.36	65.00	1.99	0.33	0.18	0.714	0.516	777.82	25.55	
CN06	392.89	850.10	72.42	0.22	46.22	65.00	1.93	0.35	0.56	0.444	0.314	453.34	15.39	
CN07	596.01	1486.6	66.79	0.11	40.09	65.00	2.36	0.37	0.22	0.609	0.441	651.10	9.24	
CAN01	102.28	108.26	95.27	0.12	94.48	62.50	1.03	0.54	0.84	0.299	0.215	81.26	20.55	
CAN02	312.43	461.86	82.95	0.23	67.65	73.95	1.37	0.76	0.17	0.299	0.215	388.57	24.37	
CAN03	72.69	110.60	97.07	0.28	65.72	79.40	2.40	0.68	0.3	0.299	0.215	73.31	0.85	
CAN04	263.02	547.91	86.30	0.22	48.00	73.95	1.50	0.71	0.67	0.299	0.215	338.82	28.82	
CAN05	72.12	176.43	84.60	0.11	40.88	62.50	1.15	0.65	0.28	0.299	0.215	117.77	63.30	
CAN06	201.15	441.24	90.82	0.19	45.59	73.95	1.67	0.66	0.85	0.299	0.215	293.30	45.81	
CAN07	283.26	673.60	84.23	0.18	42.05	73.95	1.67	0.74	0.18	0.299	0.215	299.97	5.90	
CAN08	236.61	561.35	79.83	0.25	42.15	73.95	1.82	0.79	0.22	0.299	0.215	221.63	6.33	
CAN09	255.29	1064.55	79.83	0.26	23.98	73.95	1.51	0.79	0.31	0.299	0.215	223.57	12.43	

CAN10	419.06	609.57	81.25	0.21	68.75	73.95	0.62	0.78	0.12	0.299	0.215	337.48	19.47
CL01	364.78	493.78	54.36	0.15	73.88	72.25	2.54	0.60	0.13	0.618	0.447	332.53	8.84
CL02	260.91	339.76	64.86	0.13	76.79	84.79	2.70	0.59	0.13	0.537	0.389	200.93	22.99
CL03	199.93	309.33	41.98	0.18	64.63	80.27	1.86	0.74	0.14	0.618	0.447	192.45	3.74
CL04	227.94	272.76	40.43	0.09	83.57	70.36	1.53	0.96	0.13	0.618	0.447	179.44	21.28
CL05	179.08	187.54	57.02	0.19	95.49	79.45	2.06	0.63	0.12	0.618	0.447	119.84	33.08
CL06	112.37	141.17	67.65	0.31	79.60	83.83	2.19	0.58	0.33	0.429	0.310	89.67	20.20
CL07	166.17	226.35	58.74	0.22	73.41	91.20	1.21	0.72	0.20	1.189	0.694	123.98	25.39
AMA01	179.50	307.47	90.50	0.09	58.38	17.94	1.07	0.07	0.86	0.761	0.55	223.88	24.72
AMA02	137.19	296.02	84.32	0.10	46.34	27.56	1.01	0.12	0.68	1.074	0.777	158.08	15.23
AMA03	321.21	548.11	78.67	0.30	58.60	26.58	1.03	0.12	0.77	1.203	0.870	344.32	7.19
AMA04	199.21	368.46	78.25	0.32	54.07	26.58	1.06	0.11	0.76	1.628	1.178	142.86	28.29
AMA05	320.88	445.44	77.21	0.30	72.04	18.91	0.99	0.07	0.72	0.959	0.595	281.98	12.12
AMA06	380.27	1535.06	59.22	0.13	24.77	16.86	1.46	0.12	0.20	1.074	0.777	374.47	1.53
AMA07	498.91	2419.76	68.04	0.32	20.62	29.36	1.03	0.11	0.35	1.245	0.901	658.73	32.03

Table B3. The observed mass fractions of different aerosol compositions in Beijing, China in two previous studies, as well as the assumed fractions used in this work.

Date	Particle size range	Sampler	<i>org</i> fraction	SO_4^{2-} fraction	NO_3^- fraction	NH_4^+ fraction	Cl^- fraction	Reference
Summer, 2017/2018	PM1	ACSM ^a	37%	26%	22%	14%	1%	Zhou, et al., 2019
Summer, 2018	PM2.5	ACSM	34%	31%	22%	13%	~1%	Li, et al., 2020
Summer, 2018	0.01~3um	PCASP	35%	29%	22%	13%	1%	This work

580 a. ACSM: Aerosol Chemical Speciation Monitor.

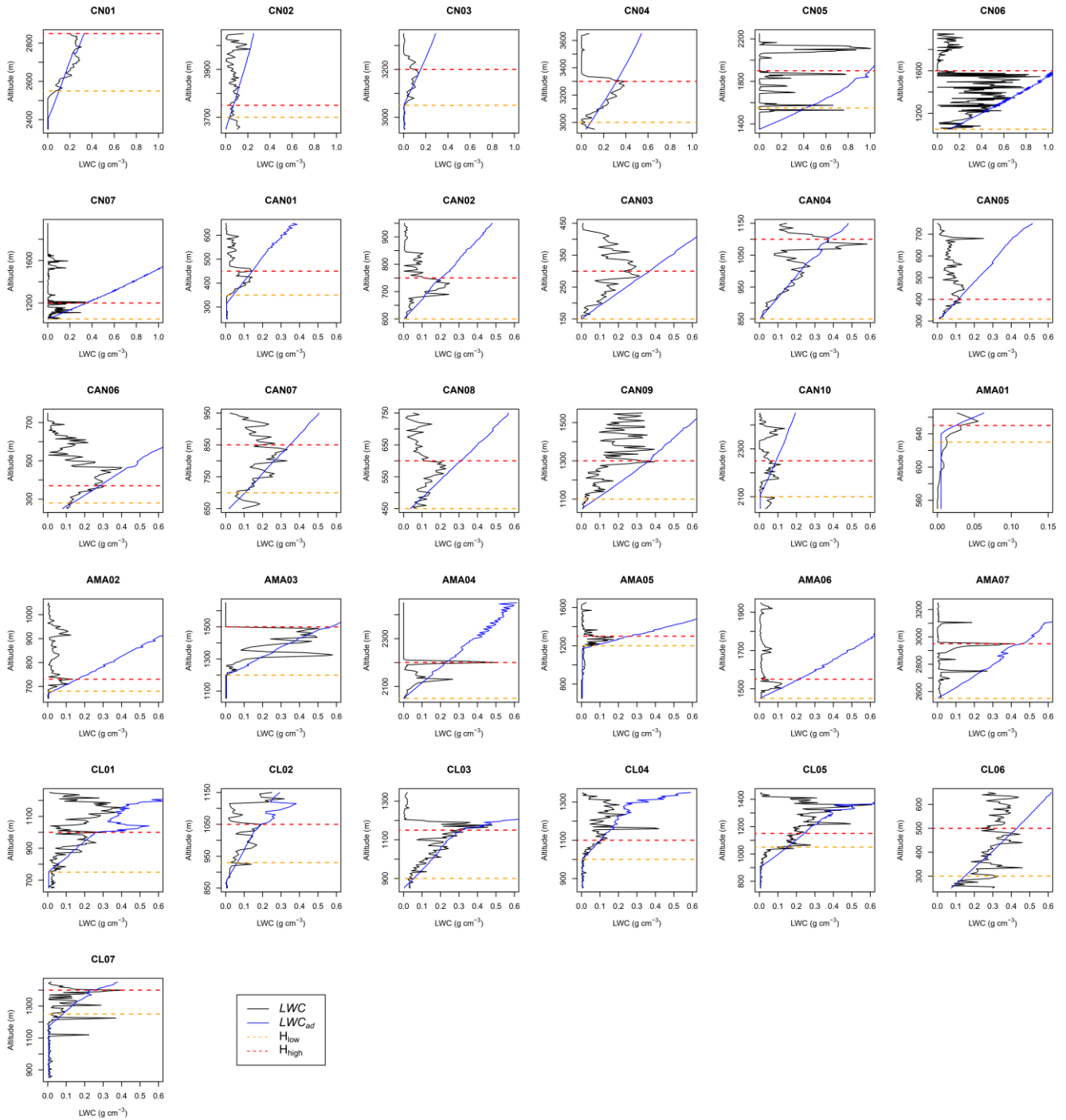
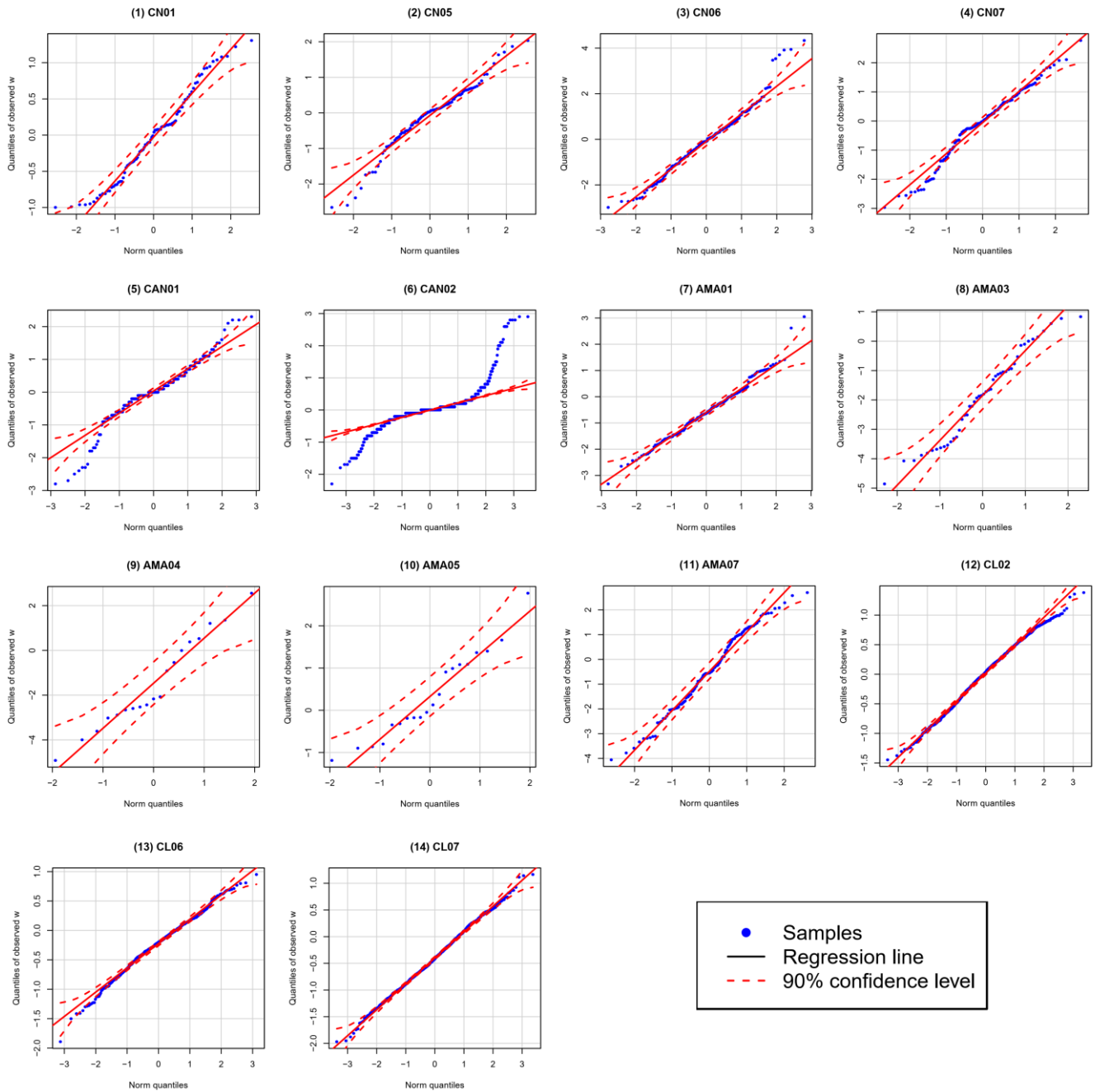


Figure B1. The profiles of observed LWC (black) and adiabatic LWC (LWC_{ad} , blue) for 31 liquid water cases.



585 **Figure B2.** The normal quantile-quantile plot for comparing the observed w sampled by aircraft with a standard normal distribution, for each cloud case with sufficient data. The linearity of the data points (blue dots) suggests that the observed w are normally distributed under a 90 % confidence level.

590 *Code and data availability.* The version of the QDGE scheme used to produce the results used in this paper, as well as the input data and scripts to run the model and the data to produce the key plot for the simulations, are archived on Zenodo and can be accessed at <https://doi.org/10.5281/zenodo.4841035> (Wang et al., 2021).

Author contribution. HW processed all data, conducted all simulations and analyses, and wrote the manuscript. YP led the work, designed the experiment, and refined the manuscript. KS developed the initial model version of the QDGE scheme and provided a summary of the approach, and contributed to the writing of the manuscript. YY, WZ, and DZ helped with the data usage in the China campaign and refined the manuscript.

595 *Competing interests.* The authors declare that they have no conflict of interest.

Acknowledgements. The authors thank VOCALS-REx and GoAmazon2014/5 for their outstanding contributions. And the high-quality data are available on VOCALS REx official website (<https://archive.eol.ucar.edu/projects/vocals/rex.html>) and Earth Observing Laboratory data (<https://data.eol.ucar.edu/dataset/89.132>). The authors are also grateful for the supports of the Beijing Weather Modification Office and the RACA campaign. In addition, we would like to thank two reviewers for their constructive suggestions to improve the manuscript. This work is supported by the National Important Project of the Ministry of Science and Technology in China (grant no. 2017YFC1501404) and the National Natural Science Foundation of China (grant nos. 42175096, 41775137, and 71690243).

References

- 605 Abdul-Razzak, H. and Ghan, S. J.: A parameterization of aerosol activation 2. Multiple aerosol types, *J. Geophys. Res. Atmos.*, 105(D5), 6837–6844, doi:10.1029/1999JD901161, 2000.
- Abdul-Razzak, H., Ghan, S. J. and Rivera-Carpio, C.: A parameterization of aerosol activation 1. Single aerosol type, *J. Geophys. Res. Atmos.*, 103(D6), 6123–6131, doi:10.1029/97JD03735, 1998.
- Albanese, D., Riccadonna, S., Donati, C. and Franceschi, P.: A practical tool for maximal information coefficient analysis, *Gigascience*, 7(4), 1–8, doi:10.1093/gigascience/giy032, 2018.
- 610 Barahona, D. and Nenes, A.: Parameterization of cloud droplet formation in large-scale models: Including effects of entrainment, *J. Geophys. Res. Atmos.*, 112(16), D16206, doi:10.1029/2007JD008473, 2007.
- Boucher, O. and Lohmann, U.: The sulfate-CCN-cloud albedo effect, *Tellus B*, 47(3), 281–300, doi:10.1034/j.1600-0889.47.issue3.1.x, 1995.
- Brenguier, J. L.: Parameterization of the condensation process: a theoretical approach, *J. Atmos. Sci.*, 48(2), 264–282, 615 doi:10.1175/1520-0469(1991)048<0264:POTCPA>2.0.CO;2, 1991.

- Chen, J., Liu, Y., Zhang, M. and Peng, Y.: New understanding and quantification of the regime dependence of aerosol-cloud interaction for studying aerosol indirect effects, *Geophys. Res. Lett.*, 43(4), 1780–1787, doi:10.1002/2016GL067683, 2016.
- Cohard, J. M., Pinty, J. P. and Suhre, K.: On the parameterization of activation spectra from cloud condensation nuclei microphysical properties, *J. Geophys. Res. Atmos.*, 105(D9), 11753–11766, doi:10.1029/1999JD901195, 2000.
- 620 Emanuel, K. A. and Hide, R.: Atmospheric Convection, *Phys. Today*, 48(4), 88–89, doi:10.1063/1.2807986, 1995.
- Ferek, R. J., Hegg, D. A., Hobbs, P. V., Durkee, P. and Nielsen, K.: Measurements of ship-induced tracks in clouds off the Washington coast, *J. Geophys. Res. Atmos.*, doi:10.1029/98JD02121, 1998.
- Flossmann, A. I., Hall, W. D. and Pruppacher, H. R.: A theoretical study of the wet removal of atmospheric pollutants. Part I: the redistribution of aerosol particles captured through nucleation and impaction scavenging by growing cloud drops., *J. Atmos. Sci.*, 42(6), 583–606, doi:10.1175/1520-0469(1985)042<0583:atsotw>2.0.co;2, 1985.
- 625 Forster, P., Storelvmo, T., Armour, K., Collins, W., Dufresne, J. L., Frame, D., Lunt, D. J., Mauritsen, T., Palmer, M. D. and Watanabe, M.: Climate Change 2021: The Physical Science Basis. Contribution of Working Group I to the Sixth Assessment Report of the Intergovernmental Panel on Climate Change, in *Climate Change 2021: The Physical Science Basis. Contribution of Working Group I to the Sixth Assessment Report of the Intergovernmental Panel on Climate Change*,
- 630 Cambridge University Press., 2021.
- Forster, P. M., Richardson, T., Maycock, A. C., Smith, C. J., Samset, B. H., Myhre, G., Andrews, T., Pincus, R. and Schulz, M.: Recommendations for diagnosing effective radiative forcing from climate models for CMIP6, *J. Geophys. Res.*, 121(20), 12,460-12,475, doi:10.1002/2016JD025320, 2016.
- Fountoukis, C. and Nenes, A.: Continued development of a cloud droplet formation parameterization for global climate models, *J. Geophys. Res. D Atmos.*, 110(11), 1–10, doi:10.1029/2004JD005591, 2005.
- 635 Fountoukis, C., Nenes, A., Meskhidze, N., Bahreini, R., Conant, W. C., Jonsson, H., Murphy, S., Sorooshian, A., Varutbangkul, V., Brechtel, F., Flagan, R. C. and Seinfeld, J. H.: Aerosol-cloud drop concentration closure for clouds sampled during the International Consortium for Atmospheric Research on Transport and Transformation 2004 campaign, *J. Geophys. Res. Atmos.*, 112(10), doi:10.1029/2006JD007272, 2007.
- 640 Gerber, H. E., Frick, G. M., Jensen, J. B. and Hudson, J. G.: Entrainment, mixing, and microphysics in trade-wind cumulus, *J. Meteorol. Soc. Japan*, 86A, 87–106, doi:10.2151/jmsj.86a.87, 2008.
- Ghan, S. J.: Technical note: Estimating aerosol effects on cloud radiative forcing, *Atmos. Chem. Phys.*, 13(19), 9971–9974, doi:10.5194/acp-13-9971-2013, 2013.
- Ghan, S. J., Abdul-Razzak, H., Nenes, A., Ming, Y., Liu, X., Ovchinnikov, M., Shipway, B., Meskhidze, N., Xu, J. and Shi, X.: Droplet nucleation: Physically-based parameterizations and comparative evaluation, *J. Adv. Model. Earth Syst.*, 3(4), doi:10.1029/2011ms000074, 2011.
- 645 Guibert, S., Snider, J. R. and Brenguier, J. L.: Aerosol activation in marine stratocumulus clouds: 1. Measurement validation for a closure study, *J. Geophys. Res. Atmos.*, 108(15), doi:10.1029/2002jd002678, 2003.

- Hallberg, A., Wobrock, W., Flossmann, A. I., Bower, K. N., Noone, K. J., Wiedensohler, A., Hansson, H. C., Wendisch, M.,
650 Berner, A., Krusiz, C., Laj, P., Facchini, M. C., Fuzzi, S. and Arends, B. G.: Microphysics of clouds: Model vs
measurements, *Atmos. Environ.*, 31(16), 2453–2462, doi:10.1016/S1352-2310(97)00041-1, 1997.
- Herrington, A. R. and Reed, K. A.: On resolution sensitivity in the Community Atmosphere Model, *Q. J. R. Meteorol. Soc.*,
146(733), 3789–3807, doi:10.1002/qj.3873, 2020.
- Jarecka, D., Pawlowska, H., Grabowski, W. W. and Wyszogrodzki, A. A.: Modeling microphysical effects of entrainment in
655 clouds observed during EUCAARI-IMPACT field campaign, *Atmos. Chem. Phys.*, 13(16), 8489–8503, doi:10.5194/acp-13-
8489-2013, 2013.
- Jones, A. and Slingo, A.: Predicting cloud-droplet effective radius and indirect sulphate aerosol forcing using a general
circulation model, *Q. J. R. Meteorol. Soc.*, 122(535), 1573–1595, doi:10.1002/qj.49712253506, 1996.
- Jones, A., Roberts, D. L. and Slingo, A.: A climate model study of indirect radiative forcing by anthropogenic sulphate
660 aerosols, *Nature*, 370(6489), 450–453, doi:10.1038/370450a0, 1994.
- Kang, I. S., Yang, Y. M. and Tao, W. K.: GCMs with implicit and explicit representation of cloud microphysics for
simulation of extreme precipitation frequency, *Clim. Dyn.*, 45(1–2), 325–335, doi:10.1007/s00382-014-2376-1, 2015.
- Khain, A. P., Beheng, K. D., Heymsfield, A., Korolev, A., Krichak, S. O., Levin, Z., Pinsky, M., Phillips, V., Prabhakaran,
T., Teller, A., Van Den Heever, S. C. and Yano, J. I.: Representation of microphysical processes in cloud-resolving models:
665 Spectral (bin) microphysics versus bulk parameterization, *Rev. Geophys.*, 53(2), 247–322, doi:10.1002/2014RG000468,
2015.
- Khvorostyanov, V. I. and Curry, J. A.: Parameterization of cloud drop activation based on analytical asymptotic solutions to
the supersaturation equation, *J. Atmos. Sci.*, 66(7), 1905–1925, doi:10.1175/2009JAS2811.1, 2009.
- Kiehl, J. T., Schneider, T. L., Rasch, P. J., Barth, M. C. and Wong, J.: Radiative forcing due to sulfate aerosols from
670 simulations with the National Center for Atmospheric Research Community Climate Model, Version 3, *J. Geophys. Res.*
Atmos., 105(D1), 1441–1457, doi:10.1029/1999JD900495, 2000.
- Kivekäs, N., Kerminen, V. M., Anttila, T., Korhonen, H., Lihavainen, H., Komppula, M. and Kulmala, M.: Parameterization
of cloud droplet activation using a simplified treatment of the aerosol number size distribution, *J. Geophys. Res. Atmos.*,
113(15), doi:10.1029/2007JD009485, 2008.
- 675 Kleinman, L. I., Daum, P. H., Lee, Y. N., Lewis, E. R., Sedlacek, A. J., Senum, G. I., Springston, S. R., Wang, J., Hubbe, J.,
Jayne, J., Min, Q., Yum, S. S. and Allen, G.: Aerosol concentration and size distribution measured below, in, and above
cloud from the DOE G-1 during VOCALS-REx, *Atmos. Chem. Phys.*, 12(1), 207–223, doi:10.5194/acp-12-207-2012, 2012.
- Kreidenweis, S. M., Petters, M. D. and Demott, P. J.: Single-parameter estimates of aerosol water content, *Environ. Res.*
Letts., 3(3), 35002–35009, doi:10.1088/1748-9326/3/3/035002, 2008.
- 680 Levy Zamora, M., Peng, J., Hu, M., Guo, S., Marrero-Ortiz, W., Shang, D., Zheng, J., Du, Z., Wu, Z. and Zhang, R.:
Wintertime aerosol properties in Beijing, *Atmos. Chem. Phys.*, 19(22), 14329–14338, doi:10.5194/acp-19-14329-2019, 2019.

- Li, S., Zhang, F., Jin, X., Sun, Y., Wu, H., Xie, C., Chen, L., Liu, J., Wu, T., Jiang, S., Cribb, M. and Li, Z.: Characterizing the ratio of nitrate to sulfate in ambient fine particles of urban Beijing during 2018–2019, *Atmos. Environ.*, 237, doi:10.1016/j.atmosenv.2020.117662, 2020.
- 685 Li, S. M., Strawbridge, K. B., Leaitch, W. R. and Macdonald, A. M.: Aerosol backscattering determined from chemical and physical properties and lidar observations over the east coast of Canada, *Geophys. Res. Lett.*, 25(10), 1653–1656, doi:10.1029/98GL00910, 1998.
- Liu, Q., Liu, D., Gao, Q., Tian, P., Wang, F., Zhao, D., Bi, K., Wu, Y., Ding, S., Hu, K., Zhang, J., Ding, D. and Zhao, C.: Vertical characteristics of aerosol hygroscopicity and impacts on optical properties over the North China Plain during winter, *Atmos. Chem. Phys.*, 20(6), 3931–3944, doi:10.5194/acp-20-3931-2020, 2020.
- 690 Lohmann, U.: Impact of sulfate aerosols on albedo and lifetime of clouds: A sensitivity study with the ECHAM4 GCM, *J. Geophys. Res. Atmos.*, 102(D12), 13685–13700, doi:10.1029/97JD00631, 1997.
- Martin, S. T., Artaxo, P., MacHado, L. A. T., Manzi, A. O., Souza, R. A. F., Schumacher, C., Wang, J., Andreae, M. O., Barbosa, H. M. J., Fan, J., Fisch, G., Goldstein, A. H., Guenther, A., Jimenez, J. L., Pöschl, U., Silva Dias, M. A., Smith, J.
- 695 N. and Wendisch, M.: Introduction: Observations and Modeling of the Green Ocean Amazon (GoAmazon2014/5), *Atmos. Chem. Phys.*, 16(8), 4785–4797, doi:10.5194/acp-16-4785-2016, 2016.
- Martin, S. T., Artaxo, P., Machado, L., Manzi, A. O., Souza, R. A. F., Schumacher, C., Wang, J., Biscaro, T., Brito, J., Calheiros, A., Jardine, K., Medeiros, A., Portela, B., De Sá S. S., Adachi, K., Aiken, A. C., Alblbrecht, R., Alexander, L., Andreae, M. O., Barbosa, H. M. J., Buseck, P., Chand, D., Comstomstock, J. M., Day, D. A., Dubey, M., Fan, J., Fastst, J.,
- 700 Fisch, G., Fortner, E., Giangrande, S., Gillles, M., Goldstein, A. H., Guenther, A., Hubbbbe, J., Jensen, M., Jimenez, J. L., Keuttsch, F. N., Kim, S., Kuang, C., Laskskin, A., McKinney, K., Mei, F., Milller, M., Nascimento, R., Pauliquevis, T., Pekour, M., Peres, J., Pet ä ä T., Pöhlkker, C., Pöschl, U., Rizzo, L., Schmid, B., Shillling, J. E., Silva Dias, M. A., Smith, J. N., Tomlmlinson, J. M., Tóta, J. and Wendisch, M.: The green ocean amazon experiment (GOAMAZON2014/5) observes pollution affecting gases, aerosols, clouds, and rainfall over the rain forest, *Bull. Am. Meteorol. Soc.*, 98(5), 981–997, doi:10.1175/BAMS-D-15-00221.1, 2017.
- 705 Menon, S., Del Genio, A. D., Koch, D. and Tselioudis, G.: GCM simulations of the aerosol indirect effect: Sensitivity to cloud parameterization and aerosol Burden, *J. Atmos. Sci.*, 59(3 PT 2), 692–713, doi:10.1175/1520-0469(2002)059<0692:gsotai>2.0.co;2, 2002.
- Meskhidze, N., Nenes, A., Conant, W. C. and Seinfeld, J. H.: Evaluation of a new cloud droplet activation parameterization with in situ data from CRYSTAL-FACE and CSTRIFE, *J. Geophys. Res. D Atmos.*, 110(16), 1–10, doi:10.1029/2004JD005703, 2005.
- 710 Ming, Y., Ramaswamy, V., Donner, L. J. and Phillips, V. T. J.: A new parameterization of cloud droplet activation applicable to general circulation models, *J. Atmos. Sci.*, 63(4), 1348–1356, doi:10.1175/JAS3686.1, 2006.

- Morrison, H. and Pinto, J. O.: Mesoscale modeling of springtime arctic mixed-phase stratiform clouds using a new two-moment bulk microphysics scheme, *J. Atmos. Sci.*, 62(10), 3683–3704, doi:10.1175/JAS3564.1, 2005.
- 715 Murray, F. W.: On the Computation of Saturation Vapor Pressure, *J. Appl. Meteorol.*, 6(1), 203–204, doi:10.1175/1520-0450(1967)006<0203:otcosv>2.0.co;2, 1967.
- Nakao, S., Tang, P., Tang, X., Clark, C. H., Qi, L., Seo, E., Asa-Awuku, A. and Cocker, D.: Density and elemental ratios of secondary organic aerosol: Application of a density prediction method, *Atmos. Environ.*, 68, 273–277, doi:10.1016/j.atmosenv.2012.11.006, 2013.
- 720 Nenes, A. and Seinfeld, J. H.: Parameterization of cloud droplet formation in global climate models, *J. Geophys. Res. Atmos.*, 108(14), doi:10.1029/2002jd002911, 2003.
- Nenes, A., Ghan, S., Abdulrazzak, H., Chuang, P. Y. and Seinfeld, J. H.: Kinetic limitations on cloud droplet formation and impact on cloud albedo, *Tellus, Ser. B Chem. Phys. Meteorol.*, doi:10.1034/j.1600-0889.2001.d01-12.x, 2001.
- 725 Pandis, S. N., Seinfeld, J. H. and Pilinis, C.: Chemical composition differences in fog and cloud droplets of different sizes, *Atmos. Environ. Part A, Gen. Top.*, 24(7), 1957–1969, doi:10.1016/0960-1686(90)90529-V, 1990.
- Peng, Y., Lohmann, U., Leaitch, R., Banic, C. and Couture, M.: The cloud albedo–cloud droplet effective radius relationship for clean and polluted clouds from RACE and FIRE.ACE, *J. Geophys. Res. Atmos.*, 107(D11), AAC 1-1–AAC 1-6, doi:10.1029/2000JD000281, 2002a.
- 730 Peng, Y., Lohmann, U., Leaitch, R., Banic, C. and Couture, M.: The cloud albedo–cloud droplet effective radius relationship for clean and polluted clouds from RACE and FIRE.ACE, *J. Geophys. Res. Atmos.*, 107(11), doi:10.1029/2000jd000281, 2002b.
- Peng, Y., Lohmann, U. and Leaitch, W. R.: Importance of vertical velocity variations in the cloud droplet nucleation process of marine stratus clouds, *J. Geophys. Res. Atmos.*, 110(21), 1–13, doi:10.1029/2004JD004922, 2005.
- 735 Petters, M. D. and Kreidenweis, S. M.: A single parameter representation of hygroscopic growth and cloud condensation nucleus activity, *Atmos. Chem. Phys.*, 7(8), 1961–1971, doi:10.5194/acp-7-1961-2007, 2007.
- Pruppacher, H. R., Klett, J. D. and Wang, P. K.: *Microphysics of Clouds and Precipitation*, *Aerosol Sci. Technol.*, 28(4), 381–382, doi:10.1080/02786829808965531, 1998.
- Reshef, D. N., Reshef, Y. A., Finucane, H. K., Grossman, S. R., McVean, G., Turnbaugh, P. J., Lander, E. S., Mitzenmacher, M. and Sabeti, P. C.: Detecting novel associations in large data sets, *Science (80-.)*, 334(6062), 1518–1524, doi:10.1126/science.1205438, 2011.
- 740 Seinfeld, J. H. and Pandis, S. N.: *Atmospheric Chemistry and Physics: From Air Pollution to Climate Change*, Third Edition, Wiley Publishing Ltd., 2016.
- Shilling, J. E., Pekour, M. S., Fortner, E. C., Artaxo, P., De Sá S., Hubbe, J. M., Longo, K. M., Machado, L. A. T., Martin, S. T., Springston, S. R., Tomlinson, J. and Wang, J.: Aircraft observations of the chemical composition and aging of aerosol in
- 745

- the Manaus urban plume during GoAmazon 2014/5, *Atmos. Chem. Phys.*, 18(14), 10773–10797, doi:10.5194/acp-18-10773-2018, 2018.
- Shipway, B. J. and Abel, S. J.: Analytical estimation of cloud droplet nucleation based on an underlying aerosol population, *Atmos. Res.*, 96(2–3), 344–355, doi:10.1016/j.atmosres.2009.10.005, 2010.
- 750 Slawinska, J., Grabowski, W. W., Pawlowska, H. and Morrison, H.: Droplet activation and mixing in large-eddy simulation of a shallow cumulus field, *J. Atmos. Sci.*, 69(2), 444–462, doi:10.1175/JAS-D-11-054.1, 2012.
- Snider, J. R. and Brenguier, J. L.: Cloud condensation nuclei and cloud droplet measurements during ACE-2, *Tellus, Ser. B Chem. Phys. Meteorol.*, 52(2), 828–842, doi:10.1034/j.1600-0889.2000.00044.x, 2000.
- Snider, J. R., Guibert, S., Brenguier, J. L. and Putaud, J. P.: Aerosol activation in marine stratocumulus clouds: 2. Köhler and
755 parcel theory closure studies, *J. Geophys. Res. Atmos.*, 108(15), doi:10.1029/2002jd002692, 2003.
- Twomey, S.: Pollution and the planetary albedo, *Atmos. Environ.*, doi:10.1016/0004-6981(74)90004-3, 1974.
- Twomey, S.: The Influence of Pollution on the Shortwave Albedo of Clouds, *J. Atmos. Sci.*, doi:10.1175/1520-0469(1977)034<1149:tiopot>2.0.co;2, 1977.
- Wang, H., Peng, Y., Salzen, K. von, Yang, Y., Zhou, W. and Zhao, D.: Evaluation of a numerically efficient aerosol
760 activation scheme by using cloud data from multiple aircraft campaigns in continental and marine regions, [data], doi:10.5281/ZENODO.4841035, 2021.
- Wang, M., Peng, Y., Liu, Y., Liu, Y., Xie, X. and Guo, Z.: Understanding Cloud Droplet Spectral Dispersion Effect Using Empirical and Semi-Analytical Parameterizations in NCAR CAM5.3, *Earth Sp. Sci.*, 7(8), e2020EA001276, doi:10.1029/2020EA001276, 2020.
- 765 Wexler, A. S. and Clegg, S. L.: Atmospheric aerosol models for systems including the ions H⁺, NH₄⁺, Na⁺, so₄²⁻, NO₃⁻, Cl⁻, Br⁻, and H₂O, *J. Geophys. Res. Atmos.*, 107(14), 4207, doi:10.1029/2001JD000451, 2002.
- Whitby, K. T.: The physical characteristics of sulfur aerosols, *Atmos. Environ.*, 12(1–3), 135–159, doi:10.1016/0004-6981(78)90196-8, 1978.
- Wood, R., Mechoso, C. R., Bretherton, C. S., Weller, R. A., Huebert, B., Straneo, F., Albrecht, B. A., Coe, H., Allen, G.,
770 Vaughan, G., Daum, P., Fairall, C., Chand, D., Gallardo Klenner, L., Garreaud, R., Grados, C., Covert, D. S., Bates, T. S., Krejci, R., Russell, L. M., De Szoek, S., Brewer, A., Yuter, S. E., Springston, S. R., Chaigneau, A., Toniazzo, T., Minnis, P., Palikonda, R., Abel, S. J., Brown, W. O. J., Williams, S., Fochesatto, J., Brioude, J. and Bower, K. N.: The VAMOS ocean-cloud-atmosphere-land study regional experiment (VOCALS-REx): Goals, platforms, and field operations, *Atmos. Chem. Phys.*, 11(2), 627–654, doi:10.5194/acp-11-627-2011, 2011.
- 775 Zhang, Y., Zhang, X., Wang, K., He, J., Leung, L. R., Fan, J. and Nenes, A.: Incorporating an advanced aerosol activation parameterization into WRF-CAM5: Model evaluation and parameterization intercomparison, *J. Geophys. Res.*, 120(14), 6952–6979, doi:10.1002/2014JD023051, 2015.

Zhou, W., Gao, M., He, Y., Wang, Q., Xie, C., Xu, W., Zhao, J., Du, W., Qiu, Y., Lei, L., Fu, P., Wang, Z., Worsnop, D. R., Zhang, Q. and Sun, Y.: Response of aerosol chemistry to clean air action in Beijing, China: Insights from two-year ACSM measurements and model simulations, *Environ. Pollut.*, 255, doi:10.1016/j.envpol.2019.113345, 2019.